



Emergence of ultrafast sparsely synchronized rhythms and their responses to external stimuli in an inhomogeneous small-world complex neuronal network



Sang-Yoon Kim, Woochang Lim*

Institute for Computational Neuroscience and Department of Science Education, Daegu National University of Education, Daegu 42411, Republic of Korea

HIGHLIGHTS

- An inhomogeneous small-world neuronal network, composed of long-range (LR) and short-range (SR) interneurons, is considered.
- Distribution of betweenness centralities, representing the effectiveness for transfer of stimulation effect, is inhomogeneous.
- Betweenness centralities of LR interneurons are much larger than those of SR interneurons.
- Effects of network architecture on emergence of sparsely synchronized rhythms are studied.
- Dynamical responses to external time-periodic stimuli are investigated in connection with betweenness centralities of stimulated interneurons.

ARTICLE INFO

Article history:

Received 18 August 2016
 Received in revised form 22 February 2017
 Accepted 11 April 2017
 Available online 28 April 2017

Keywords:

SR and LR interneurons
 Inhomogeneous small-world network
 Inhomogeneous betweenness centrality
 Ultrafast sparsely synchronized rhythms
 Synchronization suppression and enhancement

ABSTRACT

We consider an inhomogeneous small-world network (SWN) composed of inhibitory short-range (SR) and long-range (LR) interneurons, and investigate the effect of network architecture on emergence of synchronized brain rhythms by varying the fraction of LR interneurons p_{long} . The betweenness centralities of the LR and SR interneurons (characterizing the potentiality in controlling communication between other interneurons) are distinctly different. Hence, in view of the betweenness, SWNs we consider are inhomogeneous, unlike the “canonical” Watts–Strogatz SWN with nearly the same betweenness centralities. For small p_{long} , the load of communication traffic is much concentrated on a few LR interneurons. However, as p_{long} is increased, the number of LR connections (coming from LR interneurons) increases, and then the load of communication traffic is less concentrated on LR interneurons, which leads to better efficiency of global communication between interneurons. Sparsely synchronized rhythms are thus found to emerge when passing a small critical value $p_{long}^{(c)}$ ($\simeq 0.16$). The population frequency of the sparsely synchronized rhythm is ultrafast (higher than 100 Hz), while the mean firing rate of individual interneurons is much lower (~ 30 Hz) due to stochastic and intermittent neural discharges. These dynamical behaviors in the inhomogeneous SWN are also compared with those in the homogeneous Watts–Strogatz SWN, in connection with their network topologies. Particularly, we note that the main difference between the two types of SWNs lies in the distribution of betweenness centralities. Unlike the case of the Watts–Strogatz SWN, dynamical responses to external stimuli vary depending on the type of stimulated interneurons in the inhomogeneous SWN. We consider two cases of external time-periodic stimuli applied to sub-populations of the LR and SR interneurons, respectively. Dynamical responses (such as synchronization suppression and enhancement) to these two cases of stimuli are studied and discussed in relation to the betweenness centralities of stimulated interneurons, representing the effectiveness for transfer of stimulation effect in the whole network.

© 2017 Elsevier Ltd. All rights reserved.

1. Introduction

A neural circuit in the major parts of the mammalian brain consists of excitatory principal cells and inhibitory interneurons (Connors & Gutnick, 1990; Tateno, Harsch, & Robinson, 2004). The interneurons are very diverse in their morphologies and

* Corresponding author.

E-mail addresses: sykim@icn.re.kr (S.-Y. Kim), wclim@icn.re.kr (W. Lim).

functions, in contrast to the more homogeneous population of principal cells (Buzsáki, 2006; Buzsáki, Geisler, Henze, & Wang, 2004). Here, we consider the inhibitory population composed of interneurons. When the decay time of the synaptic coupling is enough long, mutual inhibition (rather than excitation) may synchronize neural firing activities (Hansel, Mato, & Meunier, 1994; van Vreewijk, Abbott, & Ermentrout, 1994). By providing a coherent oscillatory output to the principal cells, interneuronal networks play the role of the backbones of many synchronized brain rhythms (Buzsáki, 2006; Buzsáki et al., 2004; Tiesinga, Fellous, Jose, & Sejnowski, 2001; Wang, 2003, 2010; Wang & Buzsáki, 1996; Wang & Rinzler, 1992; White, Chow, Ritt, Soto-Trevino, & Kopell, 1998; Whittington, Traub, Kopell, Ermentrout, & Buhl, 2000). In this way, interneurons temporally coordinate principal neuron activity and control input and output in principal cells (Buzsáki, 2006; Buzsáki et al., 2004). A majority of short-range (SR) interneurons with mainly local connections coordinate multiple operations in principal cells, while a smaller fraction of long-range (LR) interneurons, with their axons distributed over large areas, innervate and coordinate all interneuron classes for generation of global synchrony in interneuronal networks (Bonifazi et al., 2009; Buzsáki, 2006; Buzsáki et al., 2004; Gulyás, Hájos, & Freund, 1996; Gulyás, Hájos, Katona, & Freund, 2003; Jinno et al., 2007; Melzer et al., 2012; Sik, Ylinen, Penntonen, & Buzsáki, 1994).

In this paper, we are interested in sparsely synchronized brain rhythms, associated with diverse cognitive functions (e.g., sensory perception, feature integration, selective attention, and memory formation) (Wang, 2010). At the population level, synchronous fast oscillations [e.g., fast gamma rhythm (30–100 Hz) and ultrafast sharp-wave ripple (100–200 Hz)] have been observed in local field potential recordings, while at the cellular level individual neuronal recordings have been found to exhibit stochastic and intermittent spike discharges at much lower firing rates than the population frequency like Geiger counters (Buhl, Tamas, & Fisahn, 1998; Csicsvari, Hirase, Czurko, & Buzsáki, 1998; Csicsvari, Hirase, Czurko, Mamiya, & Buzsáki, 1999; Fellous & Sejnowski, 2000; Fisahn, Pike, Buhl, & Paulsen, 1998; Fries, Reynolds, Rorie, & Desimone, 2001; Logothetis, Pauls, Augath, Trinath, & Oeltermann, 2001). For this case, only a fraction of individual neurons fires intermittently for each cycle of the population rhythm, and hence the population synchronization becomes sparse (i.e., sparse “stripes” appear in the raster plot of spikes). In this way, for the case of sparsely synchronized rhythms, single-cell firing activity differs distinctly from the population oscillatory behavior, in contrast to fully synchronized rhythms where individual neurons fire regularly at the same firing rate as the population frequency like clock oscillators (i.e., all individual neurons fire regularly for each cycle of the fully synchronized population rhythm, and hence full stripes appear in the raster plot of spikes). As examples, refer to Fig. 2(a1)–(a2) (full synchronization) and Fig. 2(b1)–(b2) (sparse synchronization) in Ref. (Kim & Lim, 2015a); fully-occupied and sparsely-occupied stripes appear in the raster plots of spikes for the full and sparse synchronizations, respectively. Under the balance between strong external excitation and strong recurrent inhibition, fast sparse synchronization was found to occur in neuronal networks for both cases of random coupling (Brunel, 2000; Brunel & Hakim, 1999; Brunel & Wang, 2003; Geisler, Brunel, & Wang, 2005) and global coupling (Brunel & Hakim, 2008; Brunel & Hansel, 2006). However, in a real neural circuit, synaptic connections are known to have complex topology which is neither regular nor completely random (Bassett & Bullmore, 2006; Bullmore & Sporns, 2009; Buzsáki et al., 2004; Chklovskii, Mel, & Svoboda, 2004; Larimer & Strowbridge, 2008; Song, Sjöström, Reigl, Nelson, & Chklovskii, 2005; Sporns, 2011; Sporns & Honey, 2006; Sporns, Tononi, & Edelman, 2000).

Here, we take into consideration the inhomogeneous population of interneurons in real neural circuits (Bonifazi et al., 2009; Buzsáki, 2006; Buzsáki et al., 2004; Gulyás et al., 1996, 2003; Jinno et al., 2007; Melzer et al., 2012; Sik et al., 1994), and consider an inhomogeneous small-world network (SWN) composed of two sub-populations of SR and LR interneurons: a preliminary computer modeling was done (Buzsáki et al., 2004; Buzsáki & Wang, 2012; Wang, 2010). Brain networks in the visual cortices of the monkeys (Felleman & van Essen, 1991; Gerhard, Pipa, Lima, Neunenschwander, & Gerstner, 2011; Young, 1993), the cats (Scannell, Burns, Hilgetag, O’Neil, & Young, 1999; Yu, Huang, Singer, & Nikolie, 2008), and the rats (Shi, Niu, & Wan, 2015) have been found to exhibit small-world properties (i.e., relatively high clustering and short path length compared to random graphs with the same number of nodes and connections) (Hilgetag, Burns, O’Neill, Scannell, & Young, 2000). Brain network architecture has likely evolved to have small-world topology, associated with low wiring cost and high dynamical complexity (Bassett & Bullmore, 2006). The Watts–Strogatz SWN model, which interpolates between regular lattice (corresponding to the case of $p_{\text{wiring}} = 0$) with high clustering and random graph (corresponding to the case of $p_{\text{wiring}} = 1$) with short path length via random uniform rewiring with the probability p_{wiring} , has been much studied (Strogatz, 2001; Watts, 2003; Watts & Strogatz, 1998). Many recent works on various subjects of neurodynamics have been done in the Watts–Strogatz SWN with predominantly local connections and rare long-distance connections (Achard & Bullmore, 2007; Kaiser & Hilgetag, 2006; Kim & Lim, 2015b; Kwon & Moon, 2002; Lago-Fernández, Huerta, Corbacho, & Sigüenza, 2000; Lizier, Pritam, & Prokopenko, 2011; Ozer, Perc, & Uzuntarla, 2009; Riecke, Roxin, Madruga, & Solla, 2007; Roxin, Riecke, & Solla, 2004; Shanahan, 2008; Sporns et al., 2000; Wang, Duan, Perc, & Chen, 2008; Wang, Perc, Duan, & Chen, 2010; Yu et al., 2008). This “canonical” Watts–Strogatz SWN is statistically homogeneous because individual interneurons have nearly same topological network centralities such as degree and betweenness. By increasing the rewiring probability p_{wiring} , LR connections come uniformly at random from all interneurons over the entire network, in contrast to real neural circuits where such LR connections are not known for the case of SR interneurons (Buzsáki et al., 2004). On the other hand, LR connections appear non-uniformly from LR interneurons in the inhomogeneous SWN we consider. For small p_{long} , LR interneurons have higher betweenness centralities B (characterizing the potentiality in controlling communication between other interneurons) than SR interneurons (Freeman, 1977, 1978), although they have the same average in- and out-degrees (i.e., the same average number of inward and outward synapses representing the potentiality in communication activity). Hence, the load of communication traffic is much concentrated on a few LR interneurons. Then, the LR interneurons tend to become overloaded by the communication traffic passing through them. For this case, it becomes difficult to get efficient communication between interneurons due to destructive interference between so many signals passing through the LR interneurons (Kim & Lim, 2015a; Nishikawa, Motter, Lai, & Hoppensteadt, 2003). However, as p_{long} is further increased, the average betweenness centrality $\langle B \rangle_{\text{LR}}$ of LR interneurons decreases due to increase in the number of LR interneurons (i.e., because the increased number of LR interneurons shares the load of communication traffic). In this way, as a result of increase in p_{long} , the average path length L_p (i.e., typical separation between two interneurons represented by average number of synapses between two interneurons along the minimal path) becomes shorter, and the load of communication traffic is less concentrated on LR interneurons because of their decreased average betweenness centrality $\langle B \rangle_{\text{LR}}$, which leads to better efficiency of global communication between interneurons.

In this paper, we study the effect of network topology such as the average path length and the betweenness centrality on emergence of ultrafast (100–200 Hz) sparsely synchronized rhythm by varying the fraction of LR interneurons p_{long} in the inhomogeneous SWN consisting of SR and LR interneurons. As examples of ultrafast sparsely synchronized rhythms, there are hippocampal sharp-wave ripples (140–200 Hz), occurring during quiet sleep and awake immobility, along with individual interneurons firing at an average rate of 30 Hz and cerebellar rhythms (150–250 Hz), associated with fine motor coordination, together with individual interneurons (Purkinje cells) firing at an average rate of 38 Hz (Brunel & Hakim, 2008; Wang, 2010). For $p_{long} = 0$, the average path length L_p is very long because there exist only SR connections, and hence global communication between distant interneurons becomes ineffective. Consequently, an unsynchronized population state appears. However, as p_{long} is increased from 0, LR connections that connect distant interneurons begin to appear non-uniformly from LR interneurons, and then the average path length L_p can be dramatically decreased only by a few short-cuts. However, in the presence of only a few LR interneurons, the load of communication traffic is much concentrated on the LR interneurons with higher betweenness centralities, and hence communication traffics passing through them occur. With further increase in p_{long} , the average betweenness centrality $\langle B \rangle_{LR}$ of LR interneurons decreases because the increased number of interneurons shares the load of communication traffic. Consequently, the load of communication traffic becomes less concentrated on the LR interneurons. Thus, global effective communication between distant interneurons may be available via LR connections. Eventually, when p_{long} passes a small critical value $p_{long}^{(c)}$ (≈ 0.16), ultrafast sparsely synchronized population rhythm emerges in the whole population because efficiency of global communication between interneurons becomes enough for occurrence of population synchronization thanks to shorter average path length L_p and smaller average betweenness centrality $\langle B \rangle_{LR}$ of LR interneurons. This transition from desynchronization to ultrafast sparse synchronization is well described in terms of a realistic “thermodynamic” order parameter, based on the instantaneous population spike rate (IPSR) kernel estimate $R(t)$ (Kim & Lim, 2014). Population synchronization emerges when R oscillates. For $p_{long} > p_{long}^{(c)}$, the IPSR kernel estimate $R(t)$ oscillates with ultrafast population frequency of 139 Hz, while individual interneurons discharge stochastic spikes at much lower rates (~ 31 Hz). This ultrafast sparse synchronization is well characterized in terms of a realistic “statistical–mechanical” spiking measure, based on R , by taking into consideration the occupation and the pacing degrees of spikes in the raster plot of spikes (Kim & Lim, 2014). With increasing p_{long} from $p_{long}^{(c)}$, the degree of ultrafast sparse synchronization increases monotonically, but its increasing rate becomes slower due to appearance of sufficient number of LR connections. These dynamical behaviors in the inhomogeneous SWN are also compared with those in the homogeneous Watts–Strogatz SWN, in connection with their network topologies.

Dynamical responses to external stimuli in the brain can provide crucial information about its dynamical properties. For example, the effects of periodic stimuli on rhythmic biological activity were experimentally studied by applying rhythmic visual stimulus (Mathewson et al., 2012) and periodic auditory stimulation (Will & Berg, 2007). Hence, it is of great importance to investigate how an external stimulus affects the neural synchronization in the brain. For the case of sparse synchronization, dynamical responses to external stimuli are found to vary depending on the type of stimulated interneurons in the inhomogeneous SWN, in contrast to the case of the Watts–Strogatz SWN (where dynamical responses have no particular dependence on randomly chosen interneurons). We consider two cases of external time-periodic stimuli applied to sub-populations of the LR and SR interneurons, respectively.

Dynamical responses to these two cases of stimuli are studied and discussed in relation to the betweenness centralities of stimulated interneurons, representing the effectiveness for transfer of stimulation effect in the whole network. It is thus found that the degree of dynamical response (e.g., synchronization suppression or enhancement) for the case of stimulated LR interneurons with higher betweenness centralities is larger (i.e., more suppressed or enhanced) than that for the case of stimulated SR interneurons with lower betweenness centralities.

This paper is organized as follows. In Section 2, we describe an inhomogeneous SWN composed of SR and LR fast spiking interneurons, and then the governing equations for the population dynamics are given. Then, in Section 3 we study the effect of network topology on emergence of ultrafast sparsely synchronized rhythms by varying p_{long} . Furthermore, we also investigate dynamical responses to external time-periodic stimuli (applied to sub-populations of the LR and SR interneurons, respectively) in connection with the betweenness centralities B of stimulated interneurons in Section 4. Finally, in Section 5, a summary is given. Explanations on methods for topological and dynamical characterizations are also made in Appendices A and B, respectively.

2. Inhomogeneous SWN composed of SR and LR fast-spiking interneurons

In this section, we first describe an inhomogeneous directed SWN composed of two sub-populations of SR and LR interneurons in Section 2.1. Then, the governing equations for the population dynamics in the inhomogeneous SWN are given in Section 2.2.

2.1. Inhomogeneous SWN

We consider an inhomogeneous directed SWN composed of N inhibitory SR and LR interneurons equidistantly placed on a one-dimensional ring of radius $N/2\pi$. The fraction of LR interneurons may be controlled by the parameter p_{long} ($0 \leq p_{long} \leq 1$). Here, we consider the case of $N = 10^3$. The connection probabilities $P(d)$ from the SR and LR interneurons are shown in Fig. 1(a). For the case of SR interneurons, the connection probability $P(d)$ from each SR interneuron to other interneurons is given by the narrow Gaussian distribution:

$$P(d) = e^{-d/2\sigma^2}, \quad (1)$$

where d represents the distance between interneurons, and σ denotes the standard deviation. On the other hand, LR interneurons are connected to other interneurons with a (slowly-decaying) power-law distribution:

$$P(d) = A(d + \kappa)^{-\alpha}. \quad (2)$$

Here, we consider the case of $\alpha = 1$, and the coefficient $A [= \sqrt{\pi/2}\sigma / (\ln(N/2 + \kappa) - \ln \kappa)]$ is determined such that the average in- and out-degrees (i.e., numbers of inward and outward connections) of the SR and LR interneurons are the same. The integrations of the connection probabilities of Eqs. (1) and (2) over all distances d [from 0 to $N/2$ (corresponding to maximum distance due to ring geometry)] give one-half of the average in- and out-degrees which are the same for both cases of the SR and LR interneurons. For the Gaussian distribution for the SR interneurons, the integration value is given by $\sqrt{\pi/2}\sigma$ because $N/2$ may be approximately replaced by ∞ for sufficiently large N . Here, we set σ to be 20 such that the average in- and out-degrees for the SR and LR interneurons become approximately 50. Fig. 1(b1) and (b2) show the histograms for the in- and out-degrees of the SR and LR interneurons for $p_{long} = 0.003$, respectively, when $N = 1000$ and $\kappa = 100$. These histograms are obtained through

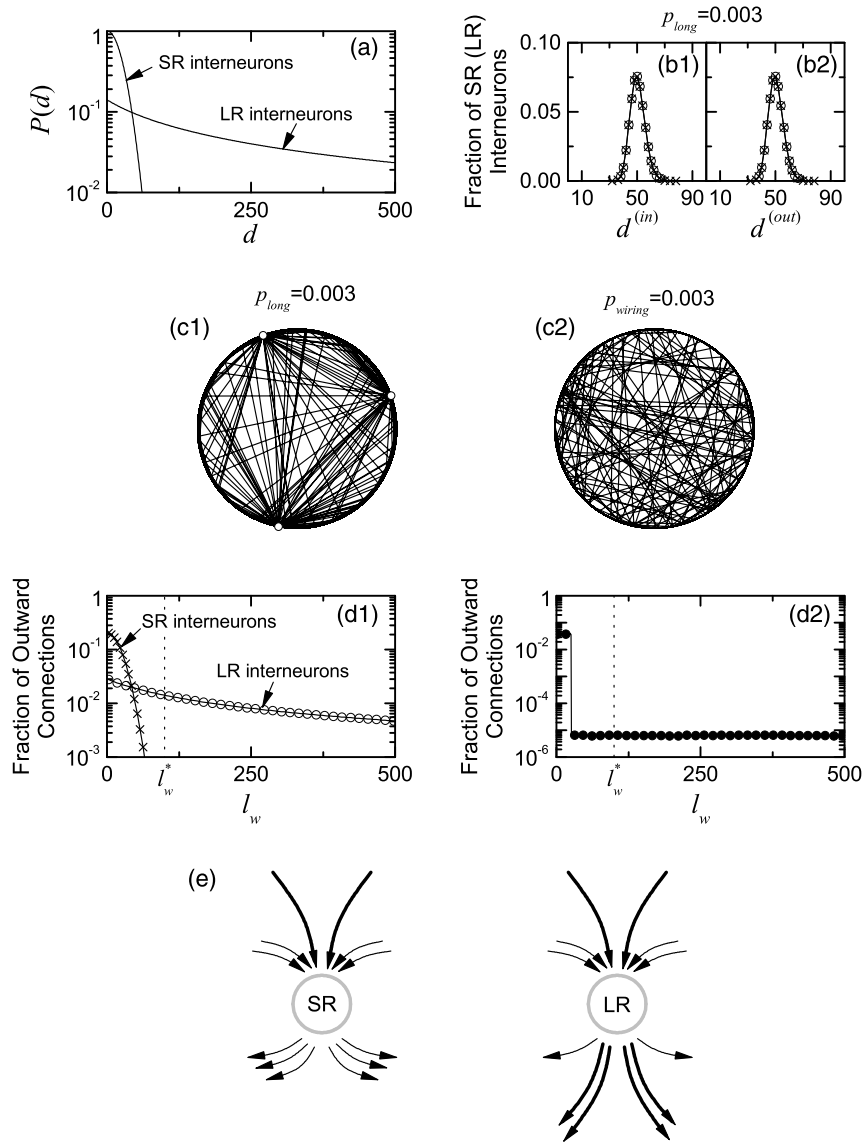


Fig. 1. Inhomogeneous SWN composed of $N(=10^3)$ SR and LR interneurons. (a) Plots of Gaussian and power-law connection probabilities $P(d)$ versus the distance d between interneurons for the SR and LR interneurons, respectively. Histograms for (b1) in- and (b2) out-degrees of the SR (crosses) and the LR (open circles) interneurons in the inhomogeneous SWN for $p_{long} = 0.003$. Synaptic connections in (c1) the inhomogeneous SWN for $p_{long} = 0.003$ (three LR interneurons are denoted by open circles) and (c2) the homogeneous Watts–Strogatz SWN [consisting of $N(=10^3)$ interneurons] for $p_{wiring} = 0.003$. Histograms for axonal wiring lengths l_w of outward connections of (d1) the SR (crosses) and the LR (open circles) interneurons in the inhomogeneous SWN for $p_{long} = 0.003$ and (d2) the interneurons (solid circles) in the homogeneous Watts–Strogatz SWN for $p_{wiring} = 0.003$. Here, $l_w^* (=100)$ is the threshold value for determining whether connections are SR or LR. (e) Schematic representation of the inward and the outward connections of the SR and LR interneurons. Long heavy solid lines denote LR connections, while others represent SR connections.

300 realizations, and the bin size for the histograms is 1. As shown well in the narrow bell-shaped distributions, the SR (crosses) and the LR (circles) interneurons have the same average in- and out-degrees whose values are 50. For comparison, we also consider the Watts–Strogatz SWN [composed of $N(=10^3)$ interneurons] with the same average number of synaptic inputs $M_{syn}(=50)$. LR connections in the inhomogeneous SWN come non-uniformly out of the LR interneurons, in contrast to the Watts–Strogatz SWN where LR connections come uniformly from all the interneurons, as shown in Fig. 1(c1) and (c2) for $p_{long} = p_{wiring} = 0.003$. Fig. 1(d1) shows histograms for axonal wiring lengths l_w of outward connections [given in Eq. (A.6)] of the SR (crosses) and the LR (circles) interneurons for $p_{long} = 0.003$. These histograms for l_w are obtained through 10^3 realizations, the bin sizes for the histograms are 1. Here, we set the threshold value $l_w^* (=100)$ for determining whether or not connections are LR, which corresponds to be twice as much as the average in- and out-degrees ($=50$). As can be

expected from the connection distributions $P(d)$, the distributions for wiring lengths l_w of outward connections for the SR (crosses) and LR (circles) interneurons are well fitted with the narrow Gaussian solid curve [$Ae^{-l_w^2/2\sigma^2}$; $A = 0.2$ and $\sigma = 20$] and the slowly-decreasing power-law solid curve [$A(l_w + 100)^{-1}$; $A = 2.8$], respectively. Hence, for the SR interneurons, only SR connections appear, while in the case of LR interneurons, about 61% of the total outward connections are LR connections. For comparison, in the case of the homogeneous Watts–Strogatz SWN with $p_{wiring} = 0.003$, the histogram for axonal wiring lengths l_w of outward connections of the interneurons is also given in Fig. 1(d2); the number of realizations for this histogram is 10^3 , and the bin size for the histogram is 1. The Watts–Strogatz SWN interpolates between the regular lattice and the random network via random uniform rewiring (Watts & Strogatz, 1998). For the case of regular network, each interneuron is connected to its first $M_{syn} (=50)$ neighbors ($M_{syn}/2$ on either side) on a ring via outward

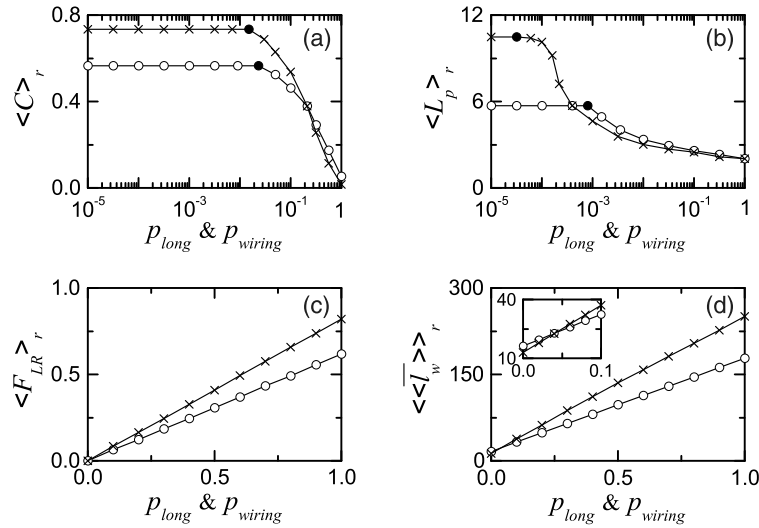


Fig. 2. Clustering coefficient C and average path length L_p in the inhomogeneous and the homogeneous Watts–Strogatz SWNs; N (total number of interneurons) for each SWN is 10^3 . Circles and crosses denote values for the cases of the inhomogeneous and homogeneous SWNs with the parameters p_{long} and p_{wiring} , respectively. (a) Plots of the clustering coefficient $\langle C \rangle_r$ versus p_{long} and p_{wiring} . (b) Plots of the average path length $\langle L_p \rangle_r$ versus p_{long} and p_{wiring} . (c) Plot of the fraction of LR outward connections $\langle F_{LR} \rangle_r$ in the whole population of interneurons versus p_{long} and p_{wiring} . (d) Plot of the ensemble-averaged mean wiring length $\langle \bar{l}_w \rangle_r$ of the outward connections in the whole population of interneurons versus p_{long} and p_{wiring} ; for more clear presentation, a magnified inset is given for small p_{long} and p_{wiring} .

connections, and then rewires each outward connection uniformly at random over the entire ring with the probability p_{wiring} such that self-connections and duplicate connections are excluded. We note that such random uniform rewiring (independent of the distance between interneurons) is in contrast to the connection probabilities (dependent on the distance) for the SR and LR interneurons in the inhomogeneous SWN. For $p_{wiring} = 0$, the wiring lengths of the total 50 000 outward connections are distributed with equal fraction ($=0.04$) in the range of $1 \leq l_w \leq 25$; otherwise, the fraction is zero. For $p_{wiring} = 0.003\%$, 0.3% of the total connections ($=150$) are rewired uniformly at random in the range of $1 \leq l_w \leq 500$ without self-connections and duplicate connections. However, the possibility that wiring lengths of the rewired connections lie in the range of $1 \leq l_w \leq 25$ is negligibly small, because the value of p_{wiring} is very small. Most of them are equally distributed in the range of $26 \leq l_w \leq 500$. Hence, the equal fraction for the wiring lengths of the outward connections in the range of $1 \leq l_w \leq 25$ is reduced to 0.0399, while the wiring lengths of the rewired connections are equally distributed with the fraction ($\simeq 6.32 \times 10^{-6}$) in the range of $26 \leq l_w \leq 500$.

For illustrative purpose, an example of the inward and the outward connections for the SR and LR interneurons is shown in Fig. 1(e). In this example, the average in- and out-degrees ($=6$) are the same for both the SR and LR interneurons. For the case of outward connections, the SR interneuron has no LR connections, while some connections ($=4$) of the LR interneuron are LR connections (denoted by long heavy solid lines). However, in the case of inward connections, there is no particular difference between the SR and LR interneurons (i.e., the LR and SR inward connections may appear for both the SR and LR interneurons). As a result, the mean wiring length \bar{l}_w of outward connections for the LR interneuron is longer than that for the SR interneuron, which might lead to some difference in the betweenness centralities B of the SR and the LR interneurons [e.g., refer to Fig. 3(b)].

2.2. Governing equations for the population dynamics

Using a Hodgkin–Huxley-type conductance-based model is biophysically accurate, but it is computationally inefficient. In contrast, using an integrate-and-fire model is computationally efficient, but it is unrealistically simple and incapable of reproducing

rich firing patterns exhibited by real biological neurons. Recently, Izhikevich introduced a simple spiking neuron model which is not only biologically plausible, but also computationally efficient (Izhikevich, 2003, 2004, 2007, 2010). Here, as an element in our SWN, we choose the fast spiking (FS) Izhikevich interneuron model. Eqs. (3)–(9) govern the population dynamics in the SWN:

$$C \frac{dv_i}{dt} = k(v_i - v_r)(v_i - v_t) - u_i + I_{DC} + D\xi_i - I_{syn,i} + S_i(t), \quad (3)$$

$$\frac{du_i}{dt} = a\{U(v_i) - u_i\}, \quad i = 1, \dots, N, \quad (4)$$

with the auxiliary after-spike resetting:

$$\text{if } v_i \geq v_p, \quad \text{then } v_i \leftarrow c \quad \text{and} \quad u_i \leftarrow u_i + d, \quad (5)$$

where

$$U(v) = \begin{cases} 0 & \text{for } v < v_b \\ b(v - v_b)^3 & \text{for } v \geq v_b, \end{cases} \quad (6)$$

$$I_{syn,i} = \frac{J}{q_i^{(in)}} \sum_{j=1(\neq i)}^N w_{ij} S_j(t) (v_i - V_{syn}), \quad (7)$$

$$S_j(t) = \sum_{f=1}^{F_j} E(t - t_f^{(j)} - \tau_i);$$

$$E(t) = \frac{1}{\tau_d - \tau_r} (e^{-t/\tau_d} - e^{-t/\tau_r}) \Theta(t), \quad (8)$$

$$S_i(t) = \alpha_i A \sin(\omega_d t). \quad (9)$$

Here, $v_i(t)$ and $u_i(t)$ are the state variables of the i th interneuron at a time t which represent the membrane potential and the recovery current, respectively. This membrane potential and the recovery variables, $v_i(t)$ and $u_i(t)$, are reset according to Eq. (5) when $v_i(t)$ reaches its cutoff value v_p . C , v_r , and v_t in Eq. (3) are the membrane capacitance, the resting membrane potential, and the instantaneous threshold potential, respectively. The parameter values used in our computations are listed in Table 1. More details on the FS Izhikevich interneuron model, the external common stimulus to all the FS interneuron, the synaptic currents, the external time-periodic stimulus to sub-populations of the LR and SR interneurons, and numerical integration of the governing equations are given in the following subsections.

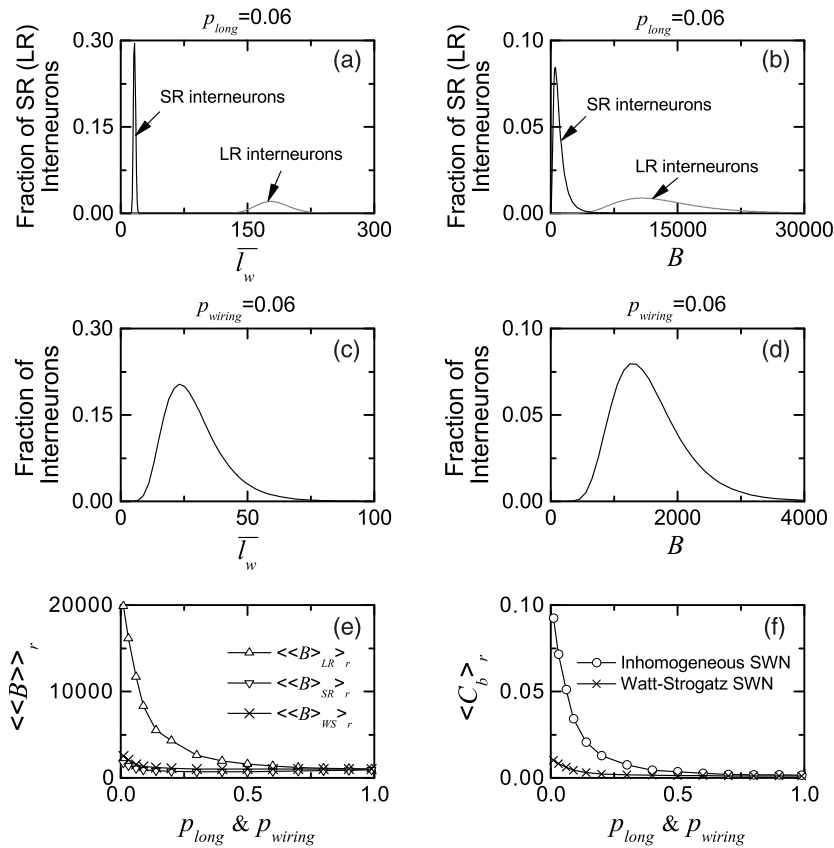


Fig. 3. Mean wiring length \bar{l}_w , betweenness centrality B , and betweenness centralization C_b . Histograms for (a) the mean wiring length \bar{l}_w of outward connections and (b) the betweenness centrality B of the SR and the LR interneurons in the inhomogeneous SWN for $p_{long} = 0.06$. Histograms for (c) the mean wiring length \bar{l}_w of outward connections and (d) the betweenness centrality B of the interneurons in the homogeneous Watts–Strogatz SWN for $p_{wiring} = 0.06$. (e) Plots of average betweenness centrality $\langle\langle B \rangle\rangle_r$ versus p_{long} and p_{wiring} ; upper and lower triangles denote the average betweenness centralities ($\langle\langle B \rangle\rangle_{LR,r}$ and $\langle\langle B \rangle\rangle_{SR,r}$) of the LR and SR interneurons, respectively, in the inhomogeneous SWN, and crosses represent the average betweenness centrality $\langle\langle B \rangle\rangle_{WS,r}$ of the interneurons in the homogeneous Watts–Strogatz SWN. (f) Plot of betweenness centralization $\langle C_b \rangle_r$ versus p_{long} and p_{wiring} ; circles and crosses represent the values in the inhomogeneous and the homogeneous Watts–Strogatz SWNs, respectively.

Table 1

Parameter values used in our computations; units of the capacitance, the potential, the current, the time, and the angular frequency are pF, mV, pA, ms, and rad/ms respectively.

(1)	Single Izhikevich FS interneurons (Izhikevich, 2007)
	$C = 20$ $v_r = -55$ $v_f = -40$ $v_p = 25$ $v_b = -55$
	$k = 1$ $a = 0.2$ $b = 0.025$ $c = -45$ $d = 0$
(2)	External common stimulus to Izhikevich FS interneurons
	$I_{DC} = 1500$ $D = 400$
(3)	Inhibitory GABAergic synapse (Brunel & Wang, 2003)
	$\tau_l = 1$ $\tau_r = 0.5$ $\tau_d = 5$ $V_{syn} = -80$
(4)	Synaptic connections between interneurons in inhomogeneous and homogeneous SWNs
	$\sigma = 20$ $\kappa = 100$ $\alpha = 1$ (inhomogeneous SWN)
	$M_{syn} = 50$ (homogeneous SWN)
	$J = 1600$
	p_{long} (inhomogeneous SWN) and p_{wiring} (homogeneous SWN): Varying
(5)	External time-periodic stimulus to the LR and SR interneurons
	$\omega_d = 0.2$ A : Varying

2.2.1. FS Izhikevich interneuron model

The Izhikevich model matches neuronal dynamics phenomenologically by tuning the parameters (k , a , b , c , d) instead of matching neuronal electrophysiology, unlike the Hodgkin–Huxley-type conductance-based models including ionic currents. The parameters k and b are related to the neuron’s rheobase and input resistance, and a , c , and d are the recovery time constant, the after-spike reset value of v , and the after-spike jump value of u , respectively.

Depending on the values of these parameters, the Izhikevich phenomenological neuron model may exhibit 20 of the most prominent neuro-computational features of cortical neurons. Here, we use the parameter values for the FS interneurons in the layer 5 rat visual cortex (Izhikevich, 2007), which are listed in the 1st item of Table 1.

2.2.2. External common stimulus to the FS Izhikevich interneuron

Each Izhikevich interneuron is stimulated by both a common DC current I_{DC} and an independent Gaussian white noise ξ_i [see the 3rd and 4th terms in Eq. (3)]. The Gaussian white noise satisfies $\langle \xi_i(t) \rangle = 0$ and $\langle \xi_i(t) \xi_j(t') \rangle = \delta_{ij} \delta(t - t')$, where $\langle \dots \rangle$ denotes the ensemble average. Here, the Gaussian noise ξ may be regarded as a parametric one which randomly perturbs the strength of the applied current I_{DC} , and its intensity is controlled by the parameter D . For $D = 0$, the Izhikevich interneuron exhibits a jump from a resting state to a spiking state via subcritical Hopf bifurcation at a higher threshold $I_{DC,h} (\simeq 73.7)$ by absorbing an unstable limit cycle born through a fold limit cycle bifurcation for a lower threshold $I_{DC,l} (\simeq 72.8)$. Hence, the Izhikevich interneuron exhibits type-II excitability because it begins to fire with a non-zero frequency (Hodgkin, 1948; Izhikevich, 2000). As I_{DC} is increased from $I_{DC,h}$, the mean firing rate f increases monotonically. The values of I_{DC} and D used in this paper are given in the 2nd item of Table 1.

2.2.3. Synaptic currents

The 5th term in Eq. (3) denotes the synaptic couplings of inhibitory FS interneurons. $I_{i,syn}$ of Eq. (7) represents the synaptic

current injected into the i th interneuron. The synaptic connectivity is given by the connection weight matrix W ($=\{w_{ij}\}$) where $w_{ij} = 1$ if the neuron j is presynaptic to the interneuron i ; otherwise, $w_{ij} = 0$. Here, the synaptic connection is modeled in terms of the inhomogeneous SWN. Among the N interneurons, LR interneurons are randomly chosen with the fraction of LR interneurons p_{long} . Then, connections from the SR and LR interneurons to other interneurons are made with the connection probabilities $P(d)$ of Eqs. (1) and (2), respectively. Through this process, the connection weight matrix W may be completed. Then, the in-degree of the i th neuron, $d_i^{(in)}$ (i.e., the number of synaptic inputs to the neuron i) is given by $d_i^{(in)} = \sum_{j=1, (j \neq i)}^N w_{ij}$. For this case, the average number of synaptic inputs per interneuron is $M_{syn} = \frac{1}{N} \sum_{i=1}^N d_i^{(in)}$.

The fraction of open synaptic ion channels at time t is denoted by $s(t)$. The time course of $s_j(t)$ of the j th interneuron is given by a sum of delayed double-exponential functions $E(t - t_f^{(j)} - \tau_i)$ [see Eq. (8)], where τ_i is the synaptic delay, and $t_f^{(j)}$ and F_j are the f th spiking time and the total number of spikes of the j th interneuron at time t , respectively. Here, $E(t)$ [which corresponds to contribution of a presynaptic spike occurring at time 0 to $s(t)$ in the absence of synaptic delay] is controlled by the two synaptic time constants: synaptic rise time τ_r and decay time τ_d , and $\Theta(t)$ is the Heaviside step function: $\Theta(t) = 1$ for $t \geq 0$ and 0 for $t < 0$. The synaptic coupling strength is controlled by the parameter J , and V_{syn} is the synaptic reversal potential. For the inhibitory GABAergic synapse (involving the GABA_A receptors), the values of τ_i , τ_r , τ_d , and V_{syn} are listed in the 3rd item of Table 1.

For comparison, we also consider the connectivity of the Watts–Strogatz SWN which interpolates between regular lattice (corresponding to the case of $p_{wiring} = 0$) and random graph (corresponding to the case of $p_{wiring} = 1$) via random uniform rewiring with the probability p_{wiring} (Strogatz, 2001; Watts, 2003; Watts & Strogatz, 1998). For $p_{wiring} = 0$, we start with a directed regular ring lattice with N FS Izhikevich interneurons where each Izhikevich interneuron is coupled to its first M_{syn} neighbors ($M_{syn}/2$ on either side) via outward synapses, and rewire each outward connection uniformly at random over the whole ring with the probability p_{wiring} (without self-connections and duplicate connections). This random uniform rewiring is made independently of the distance between interneurons, in contrast to the connection probabilities (varying depending on the distance) for the SR and LR interneurons in the inhomogeneous SWN. Here, we set $M_{syn} = 50$ which is the same as the average in-degree in the inhomogeneous SWN.

2.2.4. External time-periodic stimulus

The last term in Eq. (3) represents the external time-periodic stimulus to the i th interneuron, $S_i(t)$, the explicit form of which is given in Eq. (9). If stimulated to the i th interneuron, $\alpha_i = 1$; otherwise, $\alpha_i = 0$. (In the absence of external stimulus, $\alpha_i = 0$ for all i .) The driving angular frequency of the stimulus is ω_d , and its amplitude is A . We apply $S_i(t)$ to two sub-populations of the LR and SR interneurons with different betweenness centralities, respectively, and investigate their dynamical responses in connection with the betweenness centralities of stimulated interneurons.

2.2.5. Numerical method for integration

Numerical integration of stochastic differential equations (3)–(9) is done by employing the Heun method (San Miguel & Toral, 2000) with the time step $\Delta t = 0.01$ ms. For each realization of the stochastic process, we choose a random initial point $[v_i(0), u_i(0)]$ for the i th ($i = 1, \dots, N$) interneuron with uniform probability in the range of $v_i(0) \in (-50, -45)$ and $u_i(0) \in (10, 15)$.

3. Effect of network architecture on emergence of ultrafast sparsely synchronized rhythms in an inhomogeneous SWN

In the absence of external stimulus $S(t)$, we study the effect of network architecture on emergence of ultrafast sparsely synchronized rhythms by varying p_{long} in an inhomogeneous SWN. In Section 3.1, we first study the network topology, and then the effect of network topology on emergence of ultrafast sparsely synchronized rhythms is investigated in Section 3.2.

3.1. Topological characterization of an inhomogeneous SWN

We study the network topology of the inhomogeneous SWN in comparison with that of the Watts–Strogatz SWN; N (total number of interneurons) for each SWN is 10^3 . Methods and relevant equations for characterization of network topology and geometry are given in Appendix A. The clustering coefficient C of Eq. (A.2) (representing cliquishness of a typical neighborhood in the network) characterizes the local efficiency of information transfer, while the average path length L_p of Eq. (A.3) (denoting typical separation between two nodes in the network) characterizes the global efficiency of information transfer between distant nodes. Fig. 2(a) and (b) show plots of the clustering coefficient $\langle C \rangle_r$ and the average path length $\langle L_p \rangle_r$ versus p_{long} and p_{wiring} , respectively, in the inhomogeneous SWN (circles) and the Watts–Strogatz SWN (crosses). Hereafter, $\langle \dots \rangle_r$ represents an average over 20 realizations. For $p_{long} = p_{wiring} = 0$, both $\langle C \rangle_r$ and $\langle L_p \rangle_r$ in the inhomogeneous SWN are smaller than those in the Watts–Strogatz SWN, and this tendency continues to be valid for sufficiently small p_{long} and p_{wiring} . No LR connections appear for both cases of $p_{long} = p_{wiring} = 0$ [see Fig. 2(c)]. However, the ensemble-averaged mean geometrical wiring length $\langle \bar{l}_w \rangle$ of outward connections [given in Eq. (A.10)] coming from the SR interneurons via the Gaussian connection probability for $p_{long} = 0$ is longer than that of local connections of interneurons in the regular lattice for $p_{wiring} = 0$ [see Fig. 2(d)]; for the case of regular lattice, each interneuron is coupled to its first M_{syn} ($=50$) neighbors ($M_{syn}/2$ on either side) via outward connections on a ring. Hereafter, $\langle \dots \rangle$ denotes an ensemble average over interneurons. As a result of appearance of a little longer connections, both $\langle C \rangle_r$ and $\langle L_p \rangle_r$ become smaller for the case of $p_{long} = 0$.

As p_{long} and p_{wiring} are increased from 0, LR connections begin to appear. For the case of inhomogeneous SWN, LR connections come from LR interneurons via the power-law connection probability, while in the case of the Watts–Strogatz SWN, LR connections appear via random uniform rewiring (which is made independently of the distance between interneurons). Consequently, the fraction of LR outward connections (i.e., the ratio of the LR outward connections to the total outward connections) $\langle F_{LR} \rangle_r$ in the Watts–Strogatz SWN is larger than that in the inhomogeneous SWN, as shown in Fig. 2(c). Due to appearance of more LR connections, when passing $p_{long} = p_{wiring} \simeq 0.04$, the ensemble-averaged mean wiring length $\langle \bar{l}_w \rangle$ of outward connections for the case of Watts–Strogatz SWN becomes longer than that in the inhomogeneous SWN (i.e., a crossing occurs), as shown in the inset in Fig. 2(d).

With increasing p_{long} and p_{wiring} from 0, LR short-cuts that connect distant interneurons appear. Then, the average path length $\langle L_p \rangle_r$ may be dramatically decreased only by a few short-cuts when passing a lower threshold [$p_{long,l}^{(th)} \simeq 0.0008$ and $p_{wiring,l}^{(th)} \simeq 3 \times 10^{-5}$ which are denoted by solid circles in Fig. 2(b)], where the clustering coefficient $\langle C \rangle_r$ remains to be high. However, as a higher threshold [$p_{long,h}^{(th)} \simeq 0.023$ and $p_{wiring,h}^{(th)} \simeq 0.015$ which are also represented by solid circles in Fig. 2(a)] is passed, the cliquishness of a typical neighborhood in the network also begins

to break up due to appearance of more LR connections, and then $\langle C \rangle_r$ decreases rapidly. When the two parameters are the same (i.e., $p_{long} = p_{wiring}$), the fraction of LR outward connections $\langle F_{LR} \rangle_r$ for the case of the Watts–Strogatz SWN is larger than that for the case of inhomogeneous SWN [see Fig. 2(c)]. Hence, the effect of LR connections occurs first in the case of the Watts–Strogatz SWN. As a result, the threshold values for the Watts–Strogatz SWN become less than those for the inhomogeneous SWN. Furthermore, when passing crossing values ($p_{long} = p_{wiring} \simeq 0.0004$ for $\langle L_p \rangle_r$ and $p_{long} = p_{wiring} \simeq 0.21$ for $\langle C \rangle_r$), the values of $\langle L_p \rangle_r$ and $\langle C \rangle_r$ for the Watts–Strogatz SWN become smaller than those for the inhomogeneous SWN [i.e., crossings occur between the two curves in Fig. 2(a) and (b)]. After such crossings, due to the effect of continually increased number of LR connections, the clustering coefficient $\langle C \rangle_r$ continues to decrease rapidly, while the average path length $\langle L_p \rangle_r$ begins to decrease slowly after appearance of sufficient number of LR connections (affecting $\langle L_p \rangle_r$).

In the network science, centrality refers to indicators which identify the most important nodes within the network. In Fig. 1(b1) and (b2), we consider the simplest degree centrality, which is given by the number of edges of a node. This degree centrality represents the potentiality in communication activity. As explained above, all the SR and LR interneurons in the inhomogeneous SWN have nearly the same in- and out-degrees due to narrow bell-shaped distributions, like the case of the Watts–Strogatz SWN. Betweenness is also another centrality measure of a node within the network. Betweenness centrality B_i of Eq. (A.4) for the node i denotes the fraction of all the shortest paths between any two other nodes that pass through the node i . This betweenness centrality characterizes the potentiality in controlling communication between other interneurons. Unlike the case of the degree centrality, the distribution of betweenness centralities for the case of the inhomogeneous SWN is inhomogeneous, in contrast to the case of the Watts–Strogatz SWN with nearly same centralities. Fig. 3(a) shows histograms of the mean wiring length \bar{l}_w of outward connections for both cases of the SR and LR interneurons for $p_{long} = 0.06$. As shown in the figure with two peaks, the ensemble-averaged mean wiring length $\langle \bar{l}_w \rangle_{LR}$ ($\simeq 180.6$) over all LR interneurons is much longer than the ensemble-averaged mean wiring length $\langle \bar{l}_w \rangle_{SR}$ ($\simeq 16.3$) over all SR interneurons, because LR connections appear non-uniformly from the LR interneurons with the power-law connection probability. Although the mean wiring length is not the only factor affecting the betweenness centrality, it is expected that, in an average sense LR interneurons with longer mean wiring lengths might have larger betweenness centralities. Fig. 3(b) shows histograms of the betweenness centrality B of the SR and LR interneurons for $p_{long} = 0.06$. It is thus found that the ensemble-averaged betweenness centrality $\langle B \rangle_{LR}$ ($\simeq 13\,482$) for the case of LR interneurons is much larger than the ensemble-averaged betweenness centrality $\langle B \rangle_{SR}$ ($\simeq 1095$) for the case of SR interneurons. Hereafter, $\langle \dots \rangle_{SR}$ and $\langle \dots \rangle_{LR}$ represent the ensemble averages over the SR and LR interneurons, respectively. In this way, the two sub-populations of the SR and LR interneurons have distinctly different distributions of the betweenness centralities. For comparison, we also consider the case of the Watts–Strogatz SWN. Fig. 3(c) and (d) show the histograms of the mean wiring length \bar{l}_w and the betweenness centrality B for $p_{wiring} = 0.06$. Each histogram has only one peak, in contrast to the case of the inhomogeneous SWN with double peaks. Their ensemble-averaged values are $\langle \bar{l}_w \rangle_{WS}$ ($\simeq 28$) and $\langle B \rangle_{WS}$ ($\simeq 1574$). Hereafter, $\langle \dots \rangle_{WS}$ denotes an ensemble average over interneurons in the Watts–Strogatz SWN. These ensemble-averaged values are much smaller than those for the case of the LR interneurons, while they are a little larger than those for the case of the SR interneurons. The dispersions of the distributions in the Watts–Strogatz SWN are

also smaller than those in the whole population of the inhomogeneous SWN. All the histograms in Fig. 3(a)–(d) are obtained via 300 realizations, and the bin sizes for the histograms in Fig. 3(a)–(d) are 1, 100, 2, and 100, respectively.

By varying the parameters p_{long} and p_{wiring} , we also obtain the average betweenness centralities in Fig. 3(e). For sufficiently small p_{long} , the average betweenness centrality $\langle \langle B \rangle_{LR} \rangle_r$ (denoted by the upper triangles) of the LR interneurons is much larger than $\langle \langle B \rangle_{SR} \rangle_r$ (denoted by the lower triangles) of the SR interneurons. Consequently, load of communication traffic between interneurons is much concentrated on a few LR interneurons with higher betweenness centralities. However, as p_{long} is increased, at first $\langle \langle B \rangle_{LR} \rangle_r$ decreases very rapidly, and then its decreasing rate becomes very slow after $p_{long} \sim 0.3$. For the case of the SR interneurons, $\langle \langle B \rangle_{SR} \rangle_r$ also decreases a little, but soon it becomes nearly saturated after $p_{long} \sim 0.1$. For comparison, the average betweenness centralities $\langle \langle B \rangle_{WS} \rangle_r$ in the Watts–Strogatz SWN are also represented by crosses, and they are so close to $\langle \langle B \rangle_{SR} \rangle_r$ (but, a little larger than $\langle \langle B \rangle_{SR} \rangle_r$). For sufficiently large p_{long} and p_{wiring} (larger than about 0.9), LR interneurons become dominant, and they share the load of communication traffic. As a result, the three types of average betweenness centralities become nearly the same (i.e., the load of communication traffic is nearly evenly distributed between interneurons). To examine how evenly the betweenness centrality is distributed among interneurons (i.e., how evenly the load of communication traffic is distributed among interneurons), we consider the group betweenness centralization, representing the degree to which the maximum betweenness centrality B_{max} of the “head” LR interneuron exceeds the betweenness centralities of all the other interneurons. The betweenness centralization C_b of Eq. (A.5) is given by the sum of differences between the maximum betweenness centrality B_{max} of the head LR interneuron and the betweenness centrality B_i of other interneuron i and normalized by dividing the sum of differences with its maximum possible value. Fig. 3(f) shows plots of $\langle C_b \rangle_r$ versus p_{long} and p_{wiring} in the inhomogeneous SWN (denoted by circles) and the Watts–Strogatz SWN (represented by crosses). For small p_{long} , $\langle C_b \rangle_r$ is large, which implies that load of communication is concentrated on the head LR interneuron, and hence the head LR interneuron tends to become overloaded by the communication traffic passing through it. In this case, it becomes difficult to get efficient communication between interneurons due to destructive interference between so many signals passing through the head LR interneuron (Kim & Lim, 2015a; Nishikawa et al., 2003). However, as p_{long} is increased, $\langle C_b \rangle_r$ decreases very rapidly, and then the load of communication traffic becomes more and more evenly distributed between interneurons. In contrast, for the case of the Watts–Strogatz SWN, $\langle C_b \rangle_r$ is very small even when p_{wiring} is small. With increasing p_{wiring} , $\langle C_b \rangle_r$ decreases a little, and soon it becomes nearly saturated. Consequently, load of communication is evenly distributed between interneurons in the nearly whole range of p_{wiring} .

To summarize the network topology of the inhomogeneous SWN, as p_{long} is increased, the average path length $\langle L_p \rangle_r$ becomes shorter [see Fig. 2(b)] and load of global communication traffic becomes less concentrated on the head LR interneuron due to decrease in the betweenness centralization $\langle C_b \rangle_r$ [Fig. 3(f)] (i.e., the load of communication traffic is more evenly distributed between interneurons due to decrease in the average betweenness centrality $\langle \langle B \rangle_{LR} \rangle_r$ of LR interneurons [see Fig. 3(e)]). Consequently, with increasing p_{long} , efficiency of communication between interneurons becomes better, which may result in emergence of sparsely synchronized rhythms, as shown in Section 3.2. The inhomogeneous SWN and the Watts–Strogatz SWN have distinctly different distributions of betweenness centralities. Unlike the case of Watts–Strogatz SWN with a single-peaked distribution, the distribution of betweenness centralities in the inhomogeneous

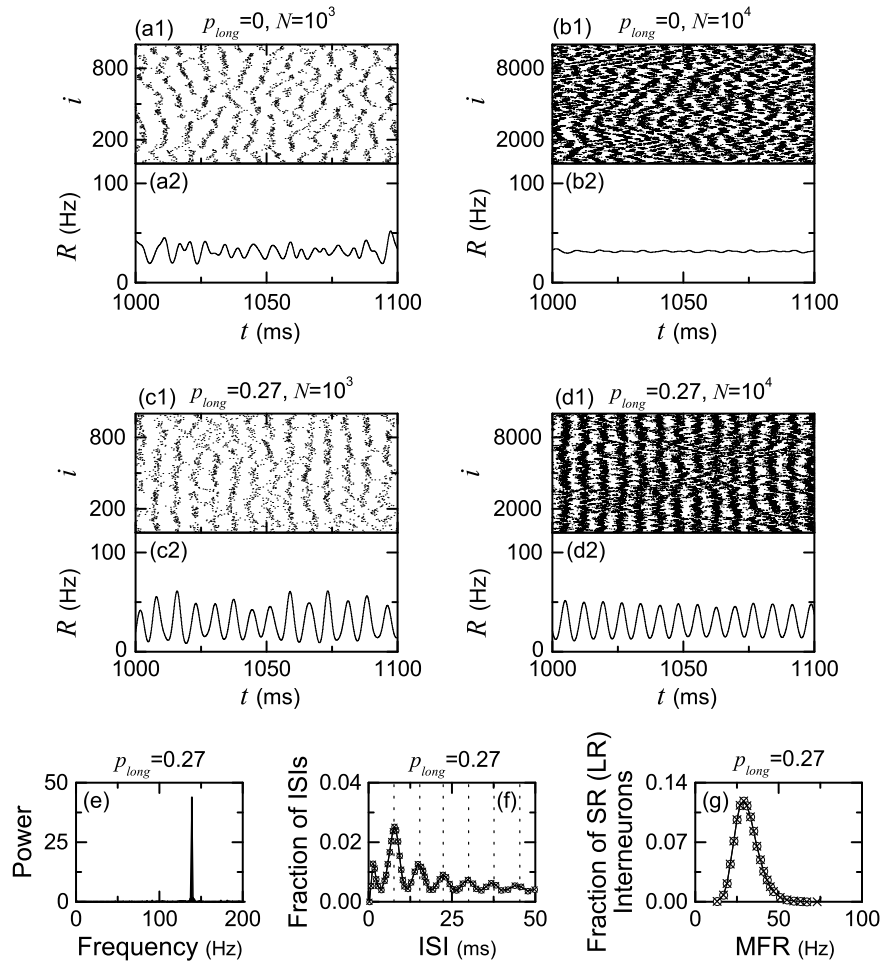


Fig. 4. Population states in the inhomogeneous SWN. Unsynchronized state for $p_{long} = 0$: raster plots of spikes for $N =$ (a1) 10^3 and (b1) 10^4 and IPSP kernel estimates $R(t)$ for $N =$ (a2) 10^3 and (b2) 10^4 . Synchronized state for $p_{long} = 0.27$: raster plots of spikes for $N =$ (c1) 10^3 and (d1) 10^4 and IPSP kernel estimates $R(t)$ for $N =$ (c2) 10^3 and (d2) 10^4 . In (e)–(g), $p_{long} = 0.27$ and $N = 10^3$. (e) One-sided power spectrum of $\Delta R(t) [= R(t) - \bar{R}(t)]$ (the overbar represents the time average) with mean-squared amplitude normalization. (f) Interspike interval (ISI) histograms of the SR and LR interneurons. Vertical dotted lines denote integer multiples of global period $T_G (\simeq 7.2$ ms) of $R(t)$. Open circles and crosses represent ISIs for the LR and SR interneurons, respectively. (g) Histograms for the mean firing rates (MFRs) of individual SR and LR interneurons. Open circles and crosses represent MFRs for the LR and SR interneurons, respectively.

SWN is double-peaked: LR interneurons have higher betweenness centralities, while SR interneurons have lower betweenness centralities. Since the betweenness centrality represents the effectiveness of information transfer, the degree of dynamical responses is expected to vary depending on whether external stimuli are applied to LR interneurons or SR interneurons, which will be investigated in Section 4.

3.2. Effect of network topology on emergence of ultrafast sparsely synchronized rhythms

In the absence of external stimulus $S(t)$, we investigate the effect of network topology on emergence of ultrafast sparsely synchronized rhythms by varying p_{long} . Methods and relevant equations for characterization of individual and population dynamics in the network composed of N interneurons are given in Appendix B. We first consider the population state for $p_{long} = 0$. As shown in Fig. 4(a1) and (a2) for $N = 10^3$, the raster plot shows a zigzag pattern intermingled with inclined partial stripes of spikes with diverse inclinations and widths, and the IPSP kernel estimate $R(t)$ of Eq. (B.2) is composed of irregular parts with fluctuating amplitudes. For $p_{long} = 0$, the clustering coefficient $\langle C \rangle_r$ in Fig. 2(a) is high, and hence partial stripes (indicating local clustering of spikes) seem to appear in the raster plot of spikes. As N is increased

to 10^4 , partial stripes become more inclined from the vertical [see Fig. 4(b1)], and then spikes become more difficult to keep pace with each other. For this case, $R(t)$ shows noisy fluctuations with smaller amplitudes, as shown in Fig. 4(b2). Consequently, the population state for $p_{long} = 0$ seems to be unsynchronized because $R(t)$ tends to be nearly stationary as N increases to the infinity. As p_{long} is increased from 0, LR connections begin to appear non-uniformly from LR interneurons. Due to the effect of these LR connections, the average path length $\langle L_p \rangle_r$ becomes shorter, and the betweenness centralization $\langle C_b \rangle_r$ becomes smaller (i.e., the load of communication traffic becomes less concentrated on LR interneurons due to decrease in the average betweenness centrality $\langle \langle B \rangle_{LR} \rangle_r$ of LR interneurons) [see Figs. 2(b), 3(e), and (f)]. Hence, with increasing p_{long} efficiency of global communication between interneurons becomes better. Eventually, when passing a critical value $p_{long}^{(c)} \simeq 0.16$, synchronized population state emerges because of sufficient efficiency of information transfer between distant interneurons, which will be discussed in more detail in Fig. 5.

As an example of a synchronized state, we consider the case of $p_{long} = 0.27$. For $N = 10^3$, the degree of zigzagness for partial stripes in the raster plot is much reduced, and hence $R(t)$ shows a regular oscillation, as shown in Fig. 4(c1)–(c2). Its amplitudes are much larger than those for $p_{long} = 0$, although there is a

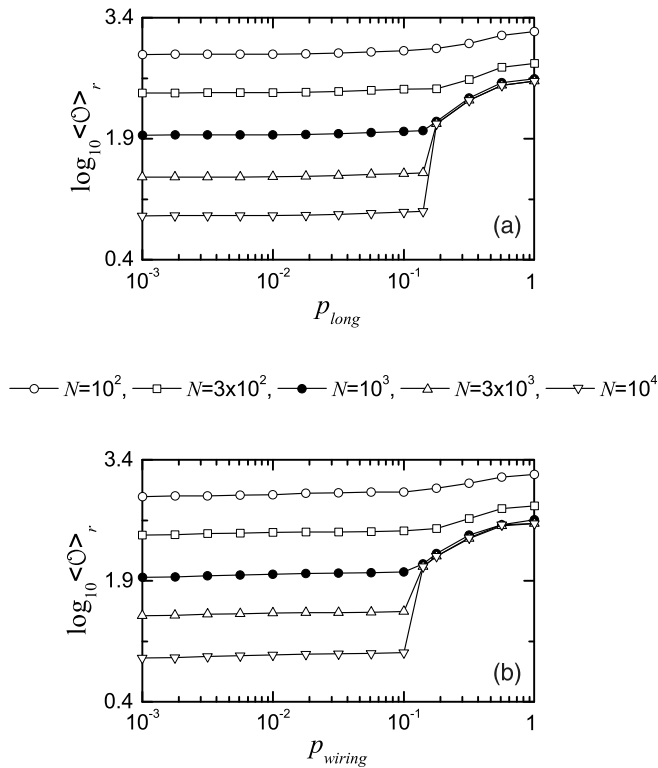


Fig. 5. Transitions from desynchronization to synchronization in the inhomogeneous and the homogeneous Watts–Strogatz SWNs. Plots of the thermodynamic order parameter $\log_{10} \langle \mathcal{O} \rangle_r$ versus (a) p_{long} and (b) p_{wiring} .

little variation in the amplitude. As N is increased to $N = 10^4$, stripes become more vertically aligned, in contrast to the case of $N = 10^3$ [see Fig. 4(d1)]. Hence, $R(t)$ shows more regular oscillations, and the amplitudes in each oscillating cycle are nearly the same, as shown in Fig. 4(d2). Consequently, the population state for $p_{long} = 0.27$ seems to be synchronized because $R(t)$ tends to show regular oscillations as N goes to the infinity. For this case, the population frequency f_p of $R(t)$ is ultrafast (about 139 Hz) [see Fig. 4(e)]. For individual behaviors of spiking interneurons, histograms for interspike intervals (ISIs) and mean firing rates (MFRs) of the LR (denoted by circles) and the SR (represented by crosses) interneurons are also shown in Fig. 4(f) and (g), respectively. Both ISI histograms of the LR and SR interneurons have multiple peaks appearing at multiples of the global period $T_G (\approx 7.2 \text{ ms})$ of $R(t)$, because the LR and SR interneurons exhibit intermittent spikings phase-locked to $R(t)$ at random multiples of the global period T_G of $R(t)$. Similar skipping phenomena of spikings (characterized with multi-peaked ISI histograms) have also been found in networks of coupled inhibitory neurons in the presence of noise where noise-induced hopping from one cluster to another one occurs (Golomb & Rinzel, 1994), in single noisy neuron models exhibiting stochastic resonance due to a weak periodic external force (Longtin, 1995, 2000), and in inhibitory networks of coupled subthreshold neurons showing stochastic spiking coherence (Kim & Lim, 2013; Lim & Kim, 2011). Due to this type of stochastic spike skipplings (i.e., random phase lockings), partial occupation occurs in the stripes of the raster plot of spikes (i.e., sparse stripes appear). Thus, the ensemble-averaged MFR $\langle \langle f_i \rangle \rangle_r (\approx 31 \text{ Hz})$ of the individual LR and SR interneurons become much lower than the population frequency $f_p (\approx 139 \text{ Hz})$, which results in the occurrence of sparse synchronization. This type of sparsely synchronized rhythms (with partially-occupied stripes of spikes) is in contrast to fully synchronized rhythms (with fully-occupied stripes) where individual neurons fire regularly at the same firing rate as the population frequency.

To determine the critical value for the desynchronization–synchronization transition, we employ a realistic thermodynamic order parameter \mathcal{O} of Eq. (B.4), given by the mean square deviation of the IPSR kernel estimate $R(t)$. For a synchronized state, $R(t)$ exhibits an oscillation with a nonzero amplitude, while in the case of desynchronization $R(t)$ becomes nearly stationary, as shown in Fig. 4. Hence, the order parameter \mathcal{O} approaches a nonzero (zero) limit value for the synchronized (unsynchronized) state in the thermodynamic limit of $N \rightarrow \infty$. Fig. 5(a) and (b) show plots of the order parameter \mathcal{O} versus p_{long} and p_{wiring} for both cases of the inhomogeneous SWN and the Watts–Strogatz SWN, respectively. For $p_{long} < p_{long}^{(c)}$ ($p_{wiring} < p_{wiring}^{(c)}$), unsynchronized states exist because the values of \mathcal{O} tend to zero as $N \rightarrow \infty$; $p_{long}^{(c)} \approx 0.16$ and $p_{wiring}^{(c)} \approx 0.12$. As p_{long} (p_{wiring}) passes the critical value $p_{long}^{(c)}$ ($p_{wiring}^{(c)}$), a transition to synchronization occurs because \mathcal{O} becomes saturated to a nonzero limit value for $N \geq 3 \times 10^3$. As explained in Section 3.1, the effect of LR connections for the Watts–Strogatz SWN is stronger than that for the inhomogeneous SWN, and hence the desynchronization–synchronization transition occurs at a smaller critical value in the case of the Watts–Strogatz SWN.

For various values of $p_{long} > p_{long}^{(c)}$, we study fast sparsely synchronized rhythms via comparison of their population behaviors with individual behaviors. As p_{long} is increased, the zigzaggness degree of partial stripes in the raster plots of spikes becomes reduced, as shown in Fig. 6(a1)–(a5), and hence the pacing degrees between spikes in the stripes become increased. Consequently, with increasing p_{long} the amplitudes of the IPSR kernel estimate $R(t)$ increase [see Fig. 6(b1)–(b5)], which implies increase in the degree of population synchronization. Fig. 6(c1)–(c5) show power spectra of $\Delta R(t) [= R(t) - \overline{R(t)}]$ (the overbar denotes the time average). For all values of p_{long} , single peaks appear at the population frequency $f_p (\approx 139 \text{ Hz})$. As p_{long} is increased, the heights of the peaks increase, while their widths decrease, thanks to the increase in the synchronization degree. As a result, with increasing p_{long} the IPSRs $R(t)$ show more and more regular oscillations with larger amplitudes at the population frequency $f_p (\approx 139 \text{ Hz})$, corresponding to the ultrafast rhythms. In contrast to fully synchronized rhythms (where individual neurons exhibit fire regularly like the clock oscillators at the same firing rate as the population frequency), the individual LR and SR interneurons exhibit stochastic and sparse discharges as Geiger counters. Fig. 6(d1)–(d5) and Fig. 6(e1)–(e5) show histograms for ISIs and MFRs of the LR (denoted by circles) and SR (represented by crosses) interneurons, respectively. Both the LR and SR interneurons exhibit intermittent spikings phase-locked to the IPSR $R(t)$ at random multiples of the global period $T_G (\approx 7.2 \text{ ms})$ of $R(t)$, and hence their ISI histograms have multiple peaks appearing at multiples of the global period T_G of $R(t)$. Due to this kind of stochastic spike skipping (i.e., random phase lockings), sparse synchronization emerges (i.e., sparse stripes appear in the raster plot of spikes). Hence, the ensemble-averaged MFR $\langle \langle f_i \rangle \rangle_r (\approx 31 \text{ Hz})$ of the LR and SR interneurons become much lower than the population frequency $f_p (\approx 139 \text{ Hz})$, which implies that the LR and SR interneurons make an average firing very sparsely about once during 4.5 global cycles. As p_{long} is increased, “valleys” (corresponding to local minima) in the ISI histograms become lowered (i.e., they become deeper), and then multiple peaks have more clear shapes. (Conversely, with decreasing p_{long} neighboring peaks overlap, and hence their shapes become less clear.) Accordingly, with increasing p_{long} the widths of the MFR distributions become reduced, and the heights of the single peaks increase (i.e., they become sharper). In this way, as p_{long} is increased stochastic spike skipping occurs in a more clear way.

By varying p_{long} in the whole range of ultrafast sparsely synchronized rhythms, we also measure the degree of ultrafast sparse synchronization in terms of a realistic statistical–mechanical spiking

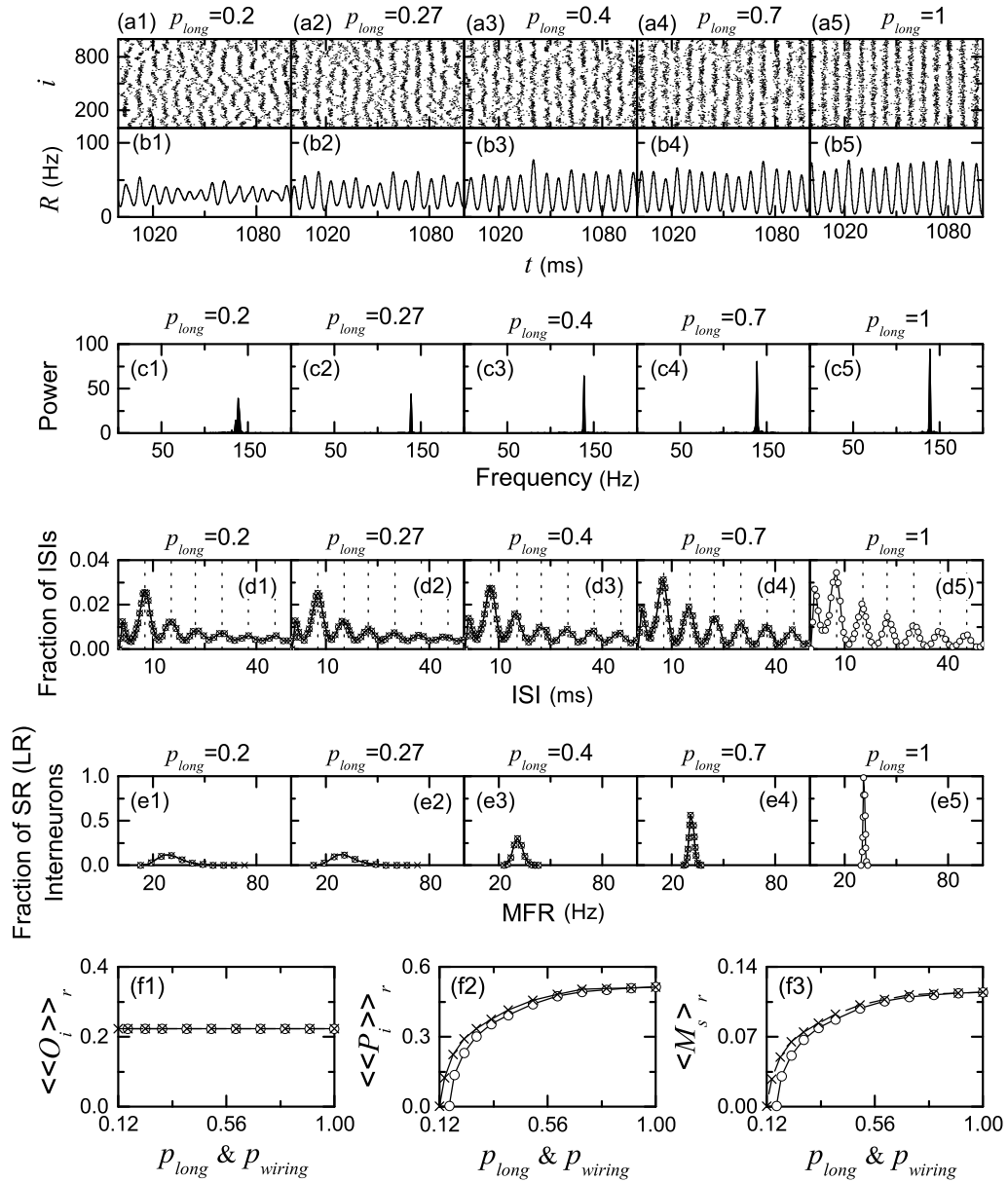


Fig. 6. Ultrafast sparsely-synchronized rhythms for various values of p_{long} in the inhomogeneous SWN with $N = 10^3$. Raster plots of neural spikes in (a1)–(a5) and IPSP kernel estimates $R(t)$ in (b1)–(b5) for various values of p_{long} . One-sided power spectrum of $\Delta R(t) [=R(t) - \langle R \rangle]$ (the overbar represents the time average) with mean-squared amplitude normalization for various values of p_{long} in (c1)–(c5). Interspike interval (ISI) histograms of the LR and SR interneurons for various values of p_{long} in (d1)–(d5) (only LR interneurons exist for $p_{long} = 1.0$). Open circles and crosses represent ISIs for the LR and SR interneurons, respectively, and vertical dotted lines denote integer multiples of global period $T_C (\simeq 7.2$ ms) of $R(t)$. Histograms for the mean firing rates (MFRs) of the individual SR and LR interneurons for various values of p_{long} = in (e1)–(e5). Open circles and crosses represent MFRs for the LR and SR interneurons, respectively. Characterization of ultrafast sparsely synchronized rhythms for $N = 10^3$: plots of (f1) the average occupation degree $\langle\langle O_i \rangle\rangle_r$, (f2) the average pacing degree $\langle\langle P_i \rangle\rangle_r$, and (f3) the statistical-mechanical spiking measure $\langle M_s \rangle_r$.

measure M_s , which was developed in our recent work (Kim & Lim, 2014). As shown in Fig. 6(a1)–(a5), population spike synchronization may be well visualized in a raster plot of spikes. For a synchronized case, the raster plot is composed of partially-occupied stripes (indicating sparse synchronization). To measure the degree of the sparse synchronization seen in the raster plot, a statistical-mechanical spiking measure M_s of Eq. (B.5), based on the IPSP kernel estimate $R(t)$, was introduced by considering the occupation degrees (representing the density of stripes) and the pacing degrees (denoting the smearing of stripes) of the spikes in the stripes (Kim & Lim, 2014): for more details on the occupation and the pacing degrees, refer to Eqs. (B.6) and (B.9) in Appendix B.4. For each p_{long} , we characterize sparse synchronization in terms of $\langle\langle O_i \rangle\rangle_r$ (average occupation degree), $\langle\langle P_i \rangle\rangle_r$ (average pacing degree), and the average statistical-mechanical spiking measure $\langle M_s \rangle_r$ via

20 realizations for various values of p_{long} in the sparsely synchronized region; in each realization, $\langle O_i \rangle_r$, $\langle P_i \rangle_r$, and M_s are obtained by following 3×10^3 stripes in the raster plot of spikes. The results (represented by circles) are shown in Fig. 6(f1)–(f3), along with the results (denoted by crosses) in the Watts–Strogatz SWN. We note that the average occupation degree $\langle\langle O_i \rangle\rangle_r$ in Fig. 6(f1) (denoting the average density of stripes in the raster plot) is nearly the same ($\langle\langle O_i \rangle\rangle_r \simeq 0.22$), independently of p_{long} . Hence, only a fraction (about 1/4.5) of the total interneurons fire in each stripe, which implies that individual interneurons fire about once during the 4.5 global cycles of the population rhythm, agreeing well with the ensemble-averaged MFR $\langle\langle f_i \rangle\rangle_r (\simeq 31$ Hz). This partial occupation in the stripes results from stochastic spike skipping of individual interneurons which is seen well in the multi-peaked ISI histograms in Fig. 6(d1)–(d5). Hence, the average occupation degree $\langle\langle O_i \rangle\rangle_r$

characterizes the sparseness degree of population synchronization well. On the other hand, as p_{long} is increased, the average pacing degree $\langle\langle P_i \rangle\rangle_r$ in Fig. 6(f2) (representing the average smearing of stripes in the raster plot) between spikes in the stripes increases due to appearance of LR connections increasing the efficiency of global communication between interneurons. However, with increasing p_{long} , the increasing rate for $\langle\langle P_i \rangle\rangle_r$ becomes slower because the effect of LR connections decreases. Fig. 6(f3) shows the average statistical–mechanical spiking measure $\langle M_s \rangle_r$ (taking into account both the occupation and the pacing degrees of spikes) versus p_{long} . Like the case of $\langle\langle P_i \rangle\rangle_r$, $\langle M_s \rangle_r$ also makes an increase, because $\langle\langle O_i \rangle\rangle_r$ is nearly independent of p_{long} . $\langle M_s \rangle_r$ is nearly equal to $\langle\langle P_i \rangle\rangle_r / 4.5$ due to sparse occupation [$\langle\langle O_i \rangle\rangle_r \simeq 0.22$]. The Watts–Strogatz SWN has more LR connections than the inhomogeneous SWN because LR connections for the Watts–Strogatz SWN appear via random uniform rewiring (which is made independently of the distance between interneurons), in contrast to the power-law connection probability (which decreases slowly with respect to the distance) for the inhomogeneous SWN. Thanks to the larger effect of these LR connections, the average statistical–mechanical spiking measure $\langle M_s \rangle_r$ of sparse synchronization in the Watts–Strogatz (denoted by crosses) is higher than that in the inhomogeneous SWN (represented by circles), as shown in Fig. 6(f1)–(f3): the average pacing degree $\langle\langle P_i \rangle\rangle_r$ for the case of the Watts–Strogatz SWN is higher, although the occupation degree $\langle\langle O_i \rangle\rangle_r$ is the same (i.e., the ensemble-averaged MFRs are the same) for both cases. However, with increasing p_{long} and p_{wiring} , the effect of LR connections decreases, and hence the difference in the synchronization degree for both cases becomes reduced.

4. Dynamical responses to external time-periodic stimuli

In this section, we study the effect of the betweenness centralities B of stimulated interneurons on the dynamical response to the external stimulus. Since B characterizes the potentiality in controlling communication between other nodes in the rest of the network, effectiveness for transfer of stimulation effect in the whole network may vary depending on B . In the inhomogeneous SWN, LR interneurons have higher betweenness centralities than SR interneurons [see Fig. 3(e)], in contrast to the homogeneous Watts–Strogatz SWN (where interneurons have nearly the same betweenness centralities). Hence, it is expected that the degree of dynamical response may be larger for the case when the external stimuli are applied to LR interneurons with higher B .

For an ultrafast sparsely synchronized case of $p_{long} = 0.27$ in Fig. 6, we apply external time-periodic stimuli $S(t) [= A \sin(\omega_d t)]$ of Eq. (9) to two sub-populations of the LR and SR interneurons with different betweenness centralities, respectively and investigate their dynamical responses (suppression or enhancement) to $S(t)$. We also discuss the differences in their responses in relation to their betweenness centralities. Dynamical responses to such external periodic driving were studied in many works (e.g., in ensembles of bursting neurons with various types of coupling Batista, Batista, de Pontes, Viana, & Lopes, 2007; Ivanchenko, Osipov, Shalfeev, & Kurths, 2004; Viana et al., 2012). Here, we set the driving angular frequency as $\omega_d (= 2\pi f_d) = 0.2$ rad/ms, corresponding to the ensemble-averaged MFR $\langle\langle f_i \rangle\rangle_r$ ($\simeq 31$ Hz) of the LR and SR interneurons [see Fig. 6(e2)]. Then, we investigate dynamical responses to $S(t)$ by varying the driving amplitude A .

We first apply $S(t)$ to $N_s (= 50)$ selected LR interneurons which have their betweenness centralities B in the range of [2502, 3043] near the ensemble-averaged betweenness centrality $\langle B \rangle_{LR}$ ($\simeq 2711$) in the ensemble of LR interneurons. By varying A , we investigate dynamical responses to $S(t)$ for a fixed $\omega_d (= 0.2)$. Here, we choose an appropriate number of stimulated interneurons as $N_s = 50$: for small $N_s \ll 50$ the stimulation effect is

very weak, and for $N_s \sim 50$ the stimulation effect becomes appreciable. Fig. 7(a1)–(a8) show raster plots of spikes for various values of A . Their corresponding IPSR kernel estimates $R(t)$ are shown in Fig. 7(b1)–(b8), and the power spectra of $\Delta R(t) [= R(t) - \overline{R(t)}]$ (the overbar represents the time average) are also given in Fig. 7(c1)–(c8). Then, the type and degree of dynamical response may be characterized in terms of a dynamical response factor D_f (Rosenblum & Pikovsky, 2004a, 2004b):

$$D_f = \sqrt{\frac{\text{Var}(R_A)}{\text{Var}(R_0)}}, \quad (10)$$

where $\text{Var}(R_A)$ and $\text{Var}(R_0)$ represent the variances of the IPSR kernel estimate $R(t)$ in the presence and absence of stimulus, respectively. If the dynamical response factor D_f is less than 1, then synchronization suppression occurs; otherwise (i.e., $D_f > 1$), synchronization enhancement takes place. Fig. 7(d) shows a plot of D_f versus A . Three stages are found to appear. Monotonic synchronization suppression (i.e., monotonic decrease in D_f from 1), decrease in synchronization suppression (i.e., increase in D_f , but still $D_f < 1$), and synchronization enhancement (i.e., increase in D_f from 1) occur in the 1st (I) stage ($0 < A < A_{1,LR}^*$), the 2nd (II) stage ($A_{1,LR}^* < A < A_{2,LR}^*$), and the 3rd (III) stage ($A > A_{2,LR}^*$), respectively; $A_{1,LR}^* \simeq 2186$ and $A_{2,LR}^* \simeq 5390$. Examples are given for various values of A ; 1st stage ($A = 400, 1000, \text{ and } 1500$), 2nd stage ($A = 4000 \text{ and } 5000$), and 3rd stage ($A = 6000, 8000, \text{ and } 10000$).

In the 1st stage, sparse stripes (which exist originally for $A = 0$) in the raster plot of spikes begin to break up due to the effect of the external AC stimulus $S(t)$. Since MFRs of stimulated interneurons increase, partially increased number of spikes appear at the sites of stimulated interneurons of the stripes, and then stripes begin to become partially horizontally scattered and merged to neighboring stripes. Many non-stimulated interneurons (i.e., major non-stimulated interneurons) which have synaptic connections with fast-firing stimulated interneurons fire slowly due to increased inhibition. On the other hand, a small number of non-stimulated interneurons (i.e. minor non-stimulated interneurons) which have no direct synaptic connections with stimulated interneurons receive synaptic inputs from major slowly-firing non-stimulated interneurons, and hence MFRs of minor non-stimulated interneurons become fast due to decreased inhibition. Consequently, the distribution of MFRs of non-stimulated interneurons becomes broadened (i.e., their dispersion increases). Due to the broadening of the MFR distribution, smearing and partial scattering occur at the sites of non-stimulated interneurons of the stripes in the raster plot of spikes. As A is increased, the degree of this type of break-up of sparse stripes increases, as shown in Fig. 7(a1)–(a3). In this 1st stage, with increasing A the amplitudes of the corresponding IPSR kernel estimates $R(t)$ decrease because of break-up of sparse stripes [see Fig. 7(b1)–(b3)]. Consequently, synchronization suppression occurs, which is well shown in the power spectra of Fig. 7(c1)–(c3). There appear two kinds of peaks in the power spectra: one is associated with ultrafast sparse synchronization and the other one is related to the external stimulus. Due to suppression of sparse synchronization, the height of the peak near 139 Hz (corresponding to ultrafast sparse synchronization) begins to decrease, and its width tends to increase. Hereafter, this type of peak will be called the “sparse-synchronization” peak. Additional main peak and its harmonics, associated with the external driving of frequency $f_d (\simeq 31$ Hz), also begin to appear. These peaks will be referred to as “stimulus” peaks. With increasing A , the heights of these stimulus peaks increase due to the increased stimulus. In this way, the degree of sparse synchronization decreases due to a destructive effect of the external AC stimulus $S(t)$ (breaking up sparse stripes).

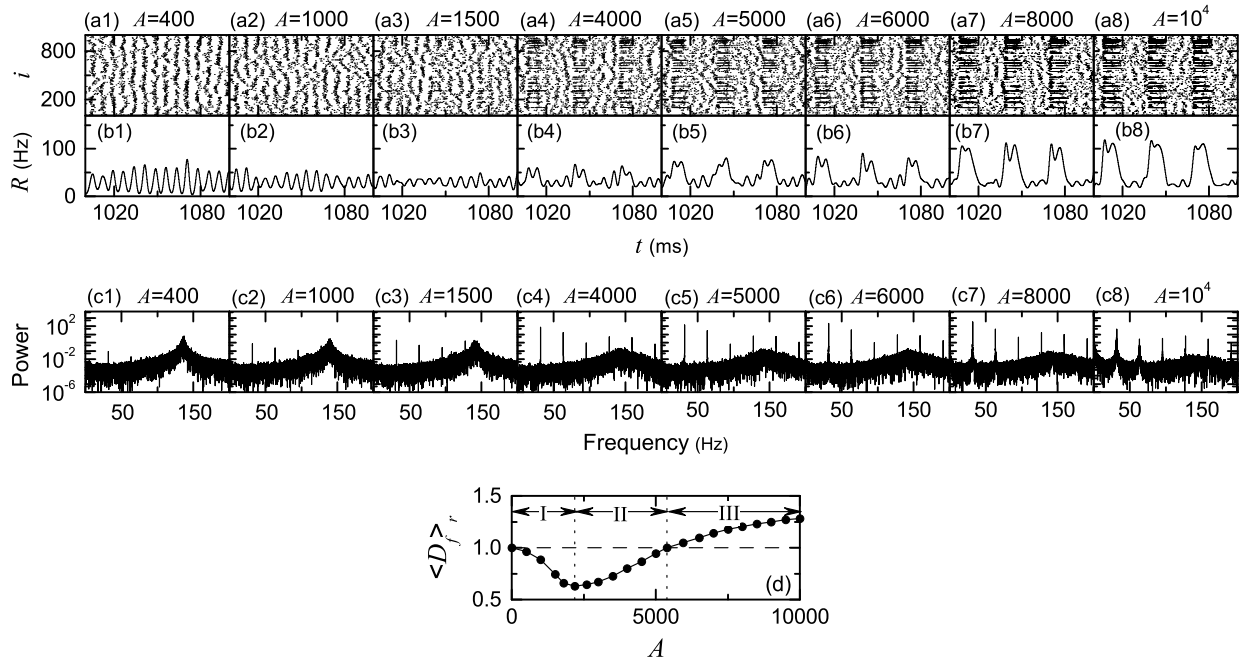


Fig. 7. Dynamical response for $p_{long} = 0.27$ when an external time-periodic stimulus $S(t)$ is applied to 50 LR interneurons with higher betweenness centralities B distributed near the average value $\langle B \rangle_{LR} (=2711)$ of the LR interneurons. Raster plots of spikes and IPSR kernel estimates $R(t)$ for various values of A are shown in (a1)–(a8) and (b1)–(b8), respectively. One-sided power spectra of $\Delta R(t) [=R(t) - \overline{R(t)}]$ (the overbar represents the time average) with mean-squared amplitude normalization are also given in (c1)–(c8). (d) Plot of dynamical response factor $\langle D_f \rangle_r$ (solid circles) versus A , where I, II, and III represent the 1st (synchronization suppression), 2nd (decrease in synchronization suppression), and 3rd (synchronization enhancement) stages, respectively.

However, when passing a threshold $A_{1,LR}^* (\simeq 2186)$, a 2nd stage occurs where synchronization suppression stops and conversely synchronization degree begins to increase. For this case, the strength of the external AC stimulus becomes moderately increased and it begins to make a constructive effect. Stimulated interneurons begin to exhibit bursting-like firing behaviors in accordance to the external AC driving. As a result, partially scattered stripes of stimulated interneurons become more and more developed and “bursting-like” bands of spikes (without “old” sparse stripes) appear successively in accordance to the external AC stimulus frequency [e.g., see Fig. 7(a4)–(a5)]. Hence, stimulated interneurons exhibit a kind of external phase lockings. With increasing A , density of spikes in the bursting-like bands increases. Within the bursting-like bands, spikes of major non-stimulated interneurons are very sparse due to strong inhibition. When getting out of a bursting-like band, inhibition is much decreased, and hence a type of “rebounding effect” occurs for the major non-stimulated interneurons. Thus, a little clear stripes, composed of increased number of spikes of non-stimulated interneurons, appear between bursting-like bands: the degree of clearness of stripes tends to increase when approaching the neighboring bursting-like band. As a whole, under the moderate strength of external AC stimulus, both appearance of bursting-like bands of stimulated interneurons and occurrence of rebounding effect outside the bands for major non-stimulated interneurons lead to increase in synchronization degree (i.e., synchronization suppression stops and then synchronization degree begins to increase). The IPSR kernel estimates $R(t)$, reflecting the structure of the raster plots of spikes, are well shown in Fig. 7(b4)–(b5). Large-amplitude oscillations appear in the regions of bursting-like bands: with increasing A , these amplitudes become larger. Due to the rebounding effect for the major non-stimulated interneurons, small-amplitude oscillations also occur outside the regions of bursting-like bands. Mainly due to the bursting-like band effect, the synchronization degree is larger than that in the 1st stage. These behaviors are well shown in the power spectra of

Fig. 7(c4)–(c5). When compared with the 1st stage, stimulus peaks, associated with the external AC stimulus, become distinct. These clear stimulus peaks are related to formation of bursting-like bands (without “original” sparse stripes). Since no original sparse stripes exist in the bursting-like bands, the overall degree in sparse synchronization decreases, although sparse stripes appear outside the bursting-like bands via the rebounding effect for the major non-stimulated interneurons. Hence, the sparse-synchronization peak near 139 Hz becomes decreased and widened. Consequently, in the 2nd stage the external AC stimulus effect becomes dominant and leads to formation of bursting-like bands of stimulated interneurons via external phase lockings. Thanks to this constructive role of the external AC stimulus, synchronization suppression (occurring in the 1st stage) stops, and conversely degree in population synchronization begins to increase.

As A is further increased, the above tendency continues. Eventually, when passing another threshold $A_{2,LR}^* (\simeq 5390)$, the dynamical response factor D_f becomes larger than unity, and hence a 3rd stage, where synchronization enhancement occurs, emerges. As shown in Fig. 7(a6)–(a8), with increasing A , bursting-like bands become more distinct due to increased density of spikes. However, spikes of major non-stimulated interneurons become much more sparse within the bursting-like bands because of increased strong inhibition. Hence, when getting out of a band, a decreased rebounding effect occurs for the major non-stimulated interneurons and less clear (i.e., more smeared) stripes appear outside the bursting-like bands when compared with the 2nd stage. Since the effect of bursting-like bands is much more dominant, overall enhancement in population synchronization occurs in the 3rd stage. The IPSR kernel estimates $R(t)$, reflecting these structures in the raster plots of spikes, are shown well in Fig. 7(b6)–(b8). As A is increased, oscillations with larger amplitudes occur in the regions of bursting-like bands. On the other hand, the amplitudes of oscillations outside the bands become smaller. Thanks to the dominant effect in the bursting-like

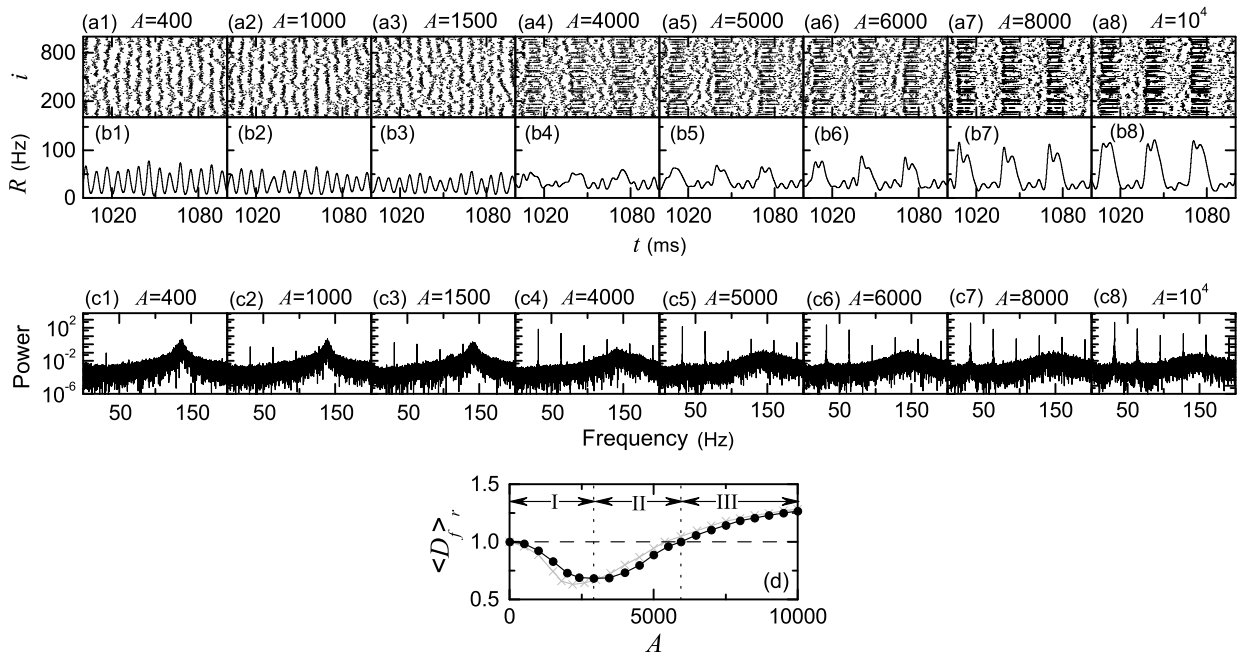


Fig. 8. Dynamical response for $p_{\text{long}} = 0.27$ when an external time-periodic stimulus $S(t)$ is applied to 50 SR interneurons with lower betweenness centralities B distributed near the average value $\langle B \rangle_{\text{SR}} (=712)$ of the SR interneurons. Raster plots of spikes and IPSR kernel estimates $R(t)$ for various values of A are shown in (a1)–(a8) and (b1)–(b8), respectively. One-sided power spectra of $\Delta R(t) [= R(t) - \overline{R}(t)]$ (the overbar represents the time average) with mean-squared amplitude normalization are also given in (c1)–(c8). (d) Plot of dynamical response factor $\langle D_f \rangle_r$ (solid circles) versus A , where I, II, and III represent the 1st (synchronization suppression), 2nd (decrease in synchronization suppression), and 3rd (synchronization enhancement) stages, respectively. For comparison, the dynamical response factor D_f (gray line) for the case of stimulated LR interneurons in Fig. 7(d) is also given.

bands, synchronization enhancement occurs. Due to the increased effect of bursting-like bands, stimulus peaks, associated with the external AC stimulus, become much more distinct. On the other hand, the sparse-synchronization peak near 139 Hz becomes more reduced, because no sparse stripes exist in the bursting-like bands and stripes outside the bands become smeared.

Based on the above results, it is found that the three stages appear through competition between the (original) ultrafast sparse (mutual) synchronization and the external phase locking. Ultrafast sparse synchronization breaks up gradually via occurrence of external phase lockings of stimulated interneurons. In the 1st stage, decrease in the sparse synchronization is dominant than the weak external phase lockings, and hence synchronization suppression occurs. However, in the 2nd stage the external phase lockings begin to be dominant. Hence, the suppression of synchronization stops, and conversely synchronization degree begins to increase. Finally, in the 3rd stage the external phase lockings become much more dominant, and consequently synchronization enhancement appears.

Next, we apply the external AC stimulus $S(t)$ to $N_s (=50)$ selected SR interneurons which have their betweenness centralities B in the range of [697, 733] near the ensemble-averaged betweenness centrality $\langle B \rangle_{\text{SR}} (\approx 712)$ in the ensemble of SR interneurons. We note that $\langle B \rangle_{\text{LR}}$ is about 3.8 times as large as $\langle B \rangle_{\text{SR}}$. Hence, transfer of stimulation effect from stimulated SR interneurons to the whole non-stimulated interneurons is expected to be less effective when compared with the case of stimulated LR interneurons. We investigate dynamical responses to $S(t)$ by varying A for a fixed $\omega_d (=0.2)$. For various values of A , raster plots of spikes, IPSR kernel estimates $R(t)$, and the power spectra of $\Delta R(t) [= R(t) - \overline{R}(t)]$ are shown in Fig. 8(a1)–(a8), (b1)–(b8), and (c1)–(c8), respectively. All of them are similar to those in Fig. 7 for the above “LR-stimulated” case. Hence, the evolution of dynamical response to $S(t)$ follows the same three stages as in the LR-stimulated case. But, due to the

difference in the effectiveness of transfer of stimulation effect, the degree of dynamical response in each stage may be different, which can be quantitatively examined in terms of the dynamical response factor D_f . A plot of D_f versus A is shown in Fig. 8(d). For comparison, D_f for the LR-stimulated case (denoted by a gray line) is also given. Since the transfer of stimulation effect to the non-stimulated interneurons is less effective, change in the degree of dynamical response is less made in a slow way. Hence, the threshold values, $A_{1,\text{SR}}^* (\approx 2921)$ and $A_{2,\text{SR}}^* (\approx 5942)$, for the 2nd and 3rd stages are larger than those for the LR-stimulated case (i.e., the 2nd and 3rd stages begin at larger threshold values due to the relatively slow evolution). Particularly, the degree of dynamical response (represented by D_f) is also reduced. In the 1st stage, the degree of synchronization suppression is less than that for the LR-stimulated case (i.e., less suppressed for the case of “SR-stimulated” case where the value of D_f is larger than that for the LR-stimulated case). In the 2nd stage, the increasing rate for D_f is larger for the LR-stimulated case, and when passing a threshold $A_{\text{cr}}^* (\approx 3163)$, the gray line (representing D_f for the LR-stimulated case) crosses the black line (denoting D_f for the SR-stimulated case). Consequently, in the 2nd and 3rd stages for $A > A_{\text{cr}}^*$, D_f for the SR-stimulated case becomes less than that for the LR-stimulated case (i.e., less enhanced for the SR-stimulated case). In this way, the degree of dynamical response (suppression or enhancement of population synchronization) is reduced because stimulated SR interneurons have lower betweenness centralities (leading to less effective transfer of stimulation effect). For sufficiently large A , the population synchronization is governed mainly by the external phase lockings of stimulated interneurons (i.e., contributions of non-stimulated interneurons to population synchronization may be negligible), and hence the two black and gray curves of D_f for both stimulated cases approach each other (i.e., synchronization enhancements for both stimulated cases become very close for sufficiently large A).

5. Summary

In contrast to the homogeneous Watts–Strogatz model, we take into consideration the inhomogeneous population of interneurons in real neural circuits: a majority of SR interneurons with mainly local connections coordinate multiple operations in principal cells, while a smaller fraction of LR interneurons, with their axons distributed over large areas, innervate and coordinate all interneuron classes for generation of population synchronization in interneuronal networks (Bonifazi et al., 2009; Buzsáki, 2006; Buzsáki et al., 2004; Gulyás et al., 1996, 2003; Jinno et al., 2007; Melzer et al., 2012; Sik et al., 1994). Thus, we considered an inhomogeneous SWN composed of the SR and LR interneurons which is more realistic in comparison with the Watts–Strogatz SWN. LR connections appear non-uniformly from the LR interneurons, in contrast to the case of the homogeneous Watts–Strogatz SWN (where LR connections appear uniformly from all interneurons). For small p_{long} , LR interneurons have higher betweenness centralities (characterizing the potentiality in controlling communication of neural signals between other interneurons) than SR interneurons. Hence, the load of communication traffic is much concentrated on a few LR interneurons. However, with further increase in p_{long} , the number of LR interneurons increases, they share load of communication traffic, and hence the average betweenness centrality $\langle B \rangle_{LR}$ of LR interneurons decreases [i.e., the (group) betweenness centralization C_b also decreases]. As a result, the average path length L_p becomes shorter, and the load of communication traffic is less concentrated on LR interneurons due to their decreased average betweenness centrality $\langle B \rangle_{LR}$ (or equivalently due to decrease in the betweenness centralization C_b), which leads to better efficiency of global communication between interneurons.

We investigated the effect of the network topology (e.g., average path length and betweenness centrality) on emergence of synchronized brain rhythms by varying p_{long} . As p_{long} is increased, effective global communication between distant interneurons begins to become available due to appearance of LR connections from the LR interneurons. Eventually, when passing a small critical value $p_{long}^{(c)} (\simeq 0.16)$, ultrafast sparsely synchronized rhythms with stochastic and intermittent neural discharges have been found to emerge because efficiency of global communication between interneurons becomes enough for occurrence of population synchronization thanks to shorter average path length L_p and smaller average betweenness centrality $\langle B \rangle_{LR}$ of LR interneurons. This transition to ultrafast sparse synchronization has been well described via calculation of the realistic thermodynamic order parameter \mathcal{O} , based on the IPSR kernel estimate $R(t)$. For $p_{long} > p_{long}^{(c)}$, the IPSR kernel estimate $R(t)$ oscillates with the ultrafast population frequency of 139 Hz, while the individual SR and LR interneurons discharge spikes stochastically at low rates (~ 31 Hz). The degree of ultrafast sparse synchronization has also been well measured in terms of the realistic statistical–mechanical spiking measure M_s . With increasing p_{long} the degree of ultrafast sparse synchronization increases, but its increasing rate becomes slower due to sufficient number of LR connections. These dynamical behaviors have also been compared with those in the Watts–Strogatz SWN, in connection with their network topologies. We note that the homogeneous Watts–Strogatz SWN has more LR connections than the inhomogeneous SWN, because LR connections for the Watts–Strogatz SWN appear via random uniform rewiring (which is made independently of the distance between interneurons), in contrast to the power-law connection probability (decreasing slowly with respect to the distance) for the inhomogeneous SWN. Thanks to the larger effect of these LR connections, ultrafast sparsely synchronized rhythms have been found to appear when passing a smaller critical value $p_{wiring}^{(c)} (\simeq 0.12)$, and the degree of sparse synchronization has also been found to become higher for the case of the

Watts–Strogatz SWN. However, with increasing p_{long} and p_{wiring} , the effect of LR connections decreases, and hence the difference in the synchronization degree for both cases becomes reduced.

Particularly, we note that the main difference between the inhomogeneous SWN and the homogeneous Watts–Strogatz SWN lies in the distributions of the betweenness centralities. Unlike the Watts–Strogatz SWN, dynamical responses to external AC stimulus vary depending on the type of stimulated interneurons (LR or SR interneurons) in the inhomogeneous SWN. We considered two cases of external AC stimuli applied to sub-populations of the LR and SR interneurons, respectively. Dynamical responses to these two cases of stimuli were investigated by varying the driving amplitude A for a fixed driving angular frequency $\omega_d (=0.2)$, and they were discussed in relation to the betweenness centralities B of stimulated interneurons, representing the effectiveness of the transfer of stimulation effect in the whole network (i.e., higher betweenness centralities imply more effectiveness for the transfer of stimulation effect). Three stages have thus been found to appear: monotonic synchronization suppression, decrease in synchronization suppression, and synchronization enhancement occur in the 1st, 2nd, and 3rd stages, respectively. The degree of dynamical response (such as synchronization suppression and enhancement) for the case of stimulated LR interneurons has been found to be larger (i.e., more suppressed or enhanced) than that for the case of stimulated SR interneurons, because stimulated LR interneurons with higher betweenness centralities make transfer of stimulation effect in the whole network more effectively in comparison with stimulated SR interneurons with lower betweenness centralities. In contrast, interneurons in the homogeneous Watts–Strogatz SWN have nearly same betweenness centralities, and hence dynamical responses to external stimuli have no particular dependence on randomly chosen interneurons. In this way, dynamical response to external stimuli is distinctly different for both cases of the inhomogeneous SWN and the Watts–Strogatz SWN, although the differences in their ultrafast sparse mutual synchronization (in the absence of external stimuli) are not significantly large. In view of practical applications, synchronization suppression may be effective in suppressing pathological brain rhythms, while synchronization enhancement might be useful for the cases of failures of cardiac or neural pacemakers. Particularly, deep brain stimulation techniques have been used to suppress pathological rhythms in patients with neural diseases such as Parkinson’s disease, essential tremor, and epilepsy (Benabid, Chabardes, Mitrofanis, & Pollak, 2009; Hamani, Neimat, & Lozano, 2006; Milton & Jung, 2003). Our results on dynamical responses to external stimuli might be useful in clinical application for controlling (i.e., suppressing or enhancing) population synchronization because such control may be more effective when time-periodic electric signal is injected to a sub-population of LR interneurons (with higher between centralities) in comparison with a sub-population of SR interneurons (with lower betweenness centralities).

Acknowledgments

This research was supported by the Basic Science Research Program through the National Research Foundation of Korea (NRF) funded by the Ministry of Education (Grant No. 2013057789).

Appendix A. Methods for characterization of network topology and geometry

In this Appendix A, methods used for characterization of topology and geometry in the network with N nodes are briefly explained.

A.1. Clustering coefficient

The clustering coefficient C_i of a node i in the network, representing the extent to which the neighborhood of the node i is clustered, may be measured by the percentage of pairs of neighbors of the node i that are also themselves neighbors (Fagiolo, 2007):

$$C_i = \frac{\text{the number of triangles in the network with the node } i \text{ as one vertex}}{\text{the number of all possible triangles that the node } i \text{ could have formed}} \quad (\text{A.1})$$

Then, the clustering coefficient C in the whole network, denoting cliquishness of a typical neighborhood in the network, is given by the average of the clustering coefficients of all nodes (Watts & Strogatz, 1998):

$$C = \frac{1}{N} \sum_{i=1}^N C_i. \quad (\text{A.2})$$

We note that C characterizes the local efficiency of information transfer: higher clustering effect occurs for large C .

A.2. Average path length

The average path length L_p , representing typical separation between two nodes in the network, is given by the average number of connections between two nodes along the shortest path (Watts & Strogatz, 1998):

$$L_p = \frac{1}{N(N-1)} \sum_{i=1}^N \sum_{j=1(j \neq i)}^N l_p^{(ij)}, \quad (\text{A.3})$$

where $l_p^{(ij)}$ is the shortest path length from the node i to the node j which may be easily obtained by employing the breadth-first searching algorithm (Brandes, 2001; Newman, 2001). We note that L_p characterizes the global efficiency of information transfer between distant nodes: global efficiency is better for shorter L_p .

A.3. Betweenness centrality and centralization

In the network science, centrality refers to indicators which identify the most important nodes within the network (i.e., the centrality indices are answers to the question “which nodes are most central?”). Historically first and conceptually simplest one is the degree centrality, which is defined by the number of edges of a node. This degree centrality represents the potentiality in communication activity. Betweenness is also another centrality measure of a node within the network (Freeman, 1977, 1978). Betweenness centrality of the node i is given by the fraction of all the shortest paths between any two other nodes that pass through the node i (Freeman, 1977, 1978):

$$B_i = \sum_{j=1(j \neq i)}^N \sum_{k=1(k \neq j \& k \neq i)}^N \frac{\sigma_{jk}(i)}{\sigma_{jk}}, \quad (\text{A.4})$$

where $\sigma_{jk}(i)$ is the number of shortest paths from the node j to the node k passing through the node i , σ_{jk} is the total number of shortest paths from the node j to the node k , and the number of shortest paths between two nodes may be easily obtained by using the breadth-first searching algorithm (Brandes, 2001; Newman, 2001). This betweenness centrality B_i characterizes the potentiality in controlling communication between other nodes in the rest of the network. In the inhomogeneous SWN, LR interneurons are found to have higher betweenness centralities than SR interneurons. Hence, the load of communication traffic is concentrated on

LR interneurons. To examine how evenly the betweenness centrality is distributed among nodes (i.e., how evenly the load of communication traffic is distributed among nodes), we consider the group betweenness centralization, denoting the degree to which the maximum betweenness centrality B_{\max} of the “head” LR interneuron exceeds the betweenness centralities of all the other interneurons. The betweenness centralization C_b is given by the sum of differences between the maximum betweenness centrality B_{\max} of the head LR interneuron and the betweenness centrality B_i of other interneuron i and normalized by dividing the sum of differences with its maximum possible value (Freeman, 1977, 1978):

$$C_b = \frac{\sum_{i=1}^N (B_{\max} - B_i)}{\max \sum_{i=1}^N (B_{\max} - B_i)}; \quad (\text{A.5})$$

$$\max \sum_{i=1}^N (B_{\max} - B_i) = \frac{(N-1)(N^2 - 3N + 2)}{2},$$

where the maximum sum of differences in the denominator corresponds to that for the star network. Large C_b implies that load of communication traffic is concentrated on the head LR interneuron, and hence the head LR interneuron tends to become overloaded by the communication traffic passing through it. For this case, it becomes difficult to get efficient communication between nodes due to destructive interference between so many signals passing through the head LR interneurons (Kim & Lim, 2015a; Nishikawa et al., 2003). On the other hand, for small C_b the load of traffic communication is less concentrated on the head LR interneuron (i.e., it is more evenly distributed between nodes), and hence efficiency of communication between nodes becomes better.

A.4. Wiring length

N interneurons are equidistantly placed on a ring of radius r ($=N/2\pi$). Then, axonal wiring length $l_w^{(ij)}$ (i.e., geometrical wiring length of connection) between node i and node j is given by the arc length between two vertices i and j on the ring (Kim & Lim, 2015a, 2015b):

$$l_w^{(ij)} = \begin{cases} |j - i| & \text{for } |j - i| \leq \frac{N}{2} \\ N - |j - i| & \text{for } |j - i| > \frac{N}{2}. \end{cases} \quad (\text{A.6})$$

Then, the total wiring length in the whole network $L_w^{(total)}$ is given by:

$$L_w^{(total)} = \sum_{i=1}^N \sum_{j=1(j \neq i)}^N a_{ij} l_w^{(ij)}, \quad (\text{A.7})$$

where a_{ij} is the ij element of the adjacency matrix A of the network. The connection between vertices in the network is denoted by its $N \times N$ adjacency matrix A ($=\{a_{ij}\}$) whose element values are 0 or 1. If $a_{ij} = 1$, then an edge from the vertex i to the vertex j exists; otherwise no such edges exist. This adjacency matrix A corresponds to the transpose of the connection weight matrix W in Section 2.2.

We are also interested in the wiring lengths of outward connections from individual interneurons. The total wiring length $l_w^{(total)}(i)$ of the outward connections from the interneuron i is given by:

$$l_w^{(total)}(i) = \sum_{j=1(j \neq i)}^N a_{ij} l_w^{(ij)}. \quad (\text{A.8})$$

Then, the mean wiring length $\overline{l_w(i)}$ of the outward connections from the interneuron i is:

$$\overline{l_w(i)} = \frac{l_w^{(total)}(i)}{N_c^{(i)}}, \quad (\text{A.9})$$

where $N_c^{(i)} (= \sum_{j=1(j \neq i)}^N a_{ij})$ is the total number of outward connections from the interneuron i . Then, the ensemble-averaged mean wiring length $\langle \overline{l_w} \rangle$ in the whole network is given by the average of the mean wiring lengths of all interneurons (Watts & Strogatz, 1998):

$$\langle \overline{l_w} \rangle = \frac{1}{N} \sum_{i=1}^N \overline{l_w(i)}. \quad (\text{A.10})$$

In the inhomogeneous SWN, the ensemble-averaged mean wiring length $\langle \overline{l_w(i)} \rangle_{LR}$ of the outward connections in the sub-population of LR interneurons is longer than $\langle \overline{l_w(i)} \rangle_{SR}$ in the sub-population of SR interneurons, because LR connections appear non-uniformly from the LR interneurons.

Appendix B. Methods for characterization of individual and population dynamics

In Appendix B, methods used for characterization of individual and population dynamics in the network of N interneurons are explained.

B.1. Characterization of individual firing behaviors

Firing behaviors of the individual SR and LR interneurons are characterized in terms of the inter-spike interval (ISI) histogram and the mean firing rate (MFR) histogram (Brunel, 2000; Brunel & Hakim, 1999, 2008; Brunel & Hansel, 2006; Brunel & Wang, 2003; Geisler et al., 2005; Kim & Lim, 2015a, 2015b). For each interneuron, 5×10^4 ISIs are collected through 50 realizations for the ISI histograms of the SR and LR interneurons, and the bin size for the histogram is 0.5 ms. The MFR for each SR or LR interneuron is calculated by following the membrane potential during the averaging time of 10^4 ms after discarding the transient time of 10^3 ms, and the bin size for the histogram is 0.5 Hz.

B.2. Population variables

In computational neuroscience, an ensemble-averaged global potential $V_G(t)$ in the whole population, containing N FS Izhikevich interneurons,

$$V_G(t) = \frac{1}{N} \sum_{i=1}^N v_i(t) \quad (\text{B.1})$$

is often used for describing emergence of population neural synchronization in the whole population (e.g., sparse synchronization in a population of subthreshold neurons was described in terms of an ensemble-averaged global potential Kim & Lim, 2013; Lim & Kim, 2011). However, to directly obtain $V_G(t)$ in real experiments is very difficult. To overcome this difficulty, instead of $V_G(t)$, we employ experimentally-obtainable instantaneous population spike rates (IPSRs) which are often used as collective quantities showing population behaviors (Brunel, 2000; Brunel & Hakim, 1999, 2008; Brunel & Hansel, 2006; Brunel & Wang, 2003; Geisler et al., 2005; Kim & Lim, 2014, 2015b; Wang, 2010). The IPSR is obtained from the raster plot of neural spikes which is a collection of spike trains of individual interneurons. Such raster plots of spikes, where population spike synchronization may be well visualized,

are fundamental data in experimental neuroscience. For the synchronous case, “stripes” (composed of spikes and indicating population synchronization) are found to be formed in the raster plot. Hence, for a synchronous case, an oscillating IPSR appears, while for an unsynchronized case the IPSR is nearly stationary. To obtain a smooth IPSR, we employ the kernel density estimation (kernel smoother) (Shimazaki & Shinomoto, 2010). Each spike in the raster plot is convoluted (or blurred) with a kernel function $K_h(t)$ to obtain a smooth estimate of IPSR $R(t)$:

$$R(t) = \frac{1}{N} \sum_{i=1}^N \sum_{s=1}^{n_i} K_h(t - t_s^{(i)}), \quad (\text{B.2})$$

where $t_s^{(i)}$ is the s th spiking time of the i th interneuron, n_i is the total number of spikes for the i th interneuron, and we use a Gaussian kernel function of band width h :

$$K_h(t) = \frac{1}{\sqrt{2\pi}h} e^{-t^2/2h^2}, \quad -\infty < t < \infty. \quad (\text{B.3})$$

Throughout the paper, the band width of the Gaussian kernel estimate is $h = 1$ ms. Moreover, for the synchronous case, the population frequency f_p of the regularly-oscillating IPSR kernel estimate $R(t)$ may be obtained from the one-sided power spectrum of $\Delta R(t)$ [$=R(t) - \overline{R(t)}$] with the mean-squared amplitude normalization. The number of data for the power spectrum is 2^{16} ($=65\,536$), and the overline represents the time average.

B.3. Thermodynamic order parameter

As is well known, a conventional order parameter, based on the ensemble-averaged global potential $V_G(t)$, is often used for describing transition from synchronization to desynchronization in computational neuroscience (Ginzburg & Sompolinsky, 1994; Hansel & Mato, 2003; Hansel & Sompolinsky, 1992; Kim & Lim, 2013; Lim & Kim, 2011). Recently, instead of the global potential, we used an experimentally-obtainable IPSR kernel estimate $R(t)$, and developed a realistic order parameter, which may be applicable in both the computational and the experimental neuroscience (Kim & Lim, 2014). The mean square deviation of the IPSR kernel estimate $R(t)$,

$$\mathcal{O} \equiv \overline{(R(t) - \overline{R(t)})^2}, \quad (\text{B.4})$$

plays the role of realistic order parameters \mathcal{O} to determine a threshold for the synchronization–desynchronization transition, where the overbar represents the time average. Here, each order parameter is obtained through average over 20 realizations, and the averaging time for the calculation of the order parameter in each realization is 3×10^4 ms. Then, the order parameter \mathcal{O} , representing the time-averaged fluctuations of $R(t)$, approaches a nonzero (zero) limit value for the synchronized (unsynchronized) state in the thermodynamic limit of $N \rightarrow \infty$. This order parameter may be regarded as a thermodynamic measure because it concerns just the macroscopic IPSR kernel estimate $R(t)$ without any consideration between the macroscopic IPSR kernel estimate and microscopic individual spikes.

B.4. Statistical–mechanical spiking measure

We measure the degree of sparse synchronization in terms of a realistic statistical–mechanical spiking measure, based on the IPSR kernel estimate $R(t)$ (Kim & Lim, 2014). Spike synchronization may be well visualized in the raster plot of spikes. For a synchronized case, the raster plot is composed of partially-occupied stripes (indicating sparse synchronization), and the corresponding IPSR kernel estimate, $R(t)$, exhibits a regular oscillation. Each i th ($i =$

1, 2, 3, ...) global cycle of $R(t)$ begins from its left minimum, passes the central maximum, and ends at the right minimum [also, corresponding to the beginning point of the next $(i + 1)$ th global cycle]; the 1st global cycle of $R(t)$ appears after transient times of 10^3 ms. Spikes which appear in the i th global cycle of $R(t)$ form the i th stripe in the raster plot. To measure the degree of spike synchronization seen in the raster plot, a statistical–mechanical measure M_s , based on $R(t)$, was introduced by considering the occupation pattern and the pacing pattern of spikes in the stripes (Kim & Lim, 2014). The spiking measure M_i of the i th stripe [appearing in the i th global cycle of $R(t)$] is defined by the product of the occupation degree O_i of spikes (representing the density of the i th stripe) and the pacing degree P_i of spikes (denoting the smearing of the i th stripe):

$$M_i = O_i \cdot P_i. \quad (\text{B.5})$$

The occupation degrees O_i in the i th stripe are given by the fractions of spiking interneurons in the i th stripe:

$$O_i = \frac{N_i^{(s)}}{N}, \quad (\text{B.6})$$

where $N_i^{(s)}$ is the number of spiking interneurons in the i th stripe. For sparse synchronization with partially-occupied stripes, $O_i \ll 1$. The pacing degree P_i of sparse spikes in the i th stripe can be determined in a statistical–mechanical way by taking into account their contributions to the macroscopic IPSR kernel estimate $R(t)$. An instantaneous global phase $\Phi(t)$ of $R(t)$ was introduced via linear interpolation in the two successive subregions forming global cycles (Kim & Lim, 2014). The global phase $\Phi(t)$ between the left minimum (corresponding to the beginning point of the i th global cycle) and the central maximum is given by

$$\Phi(t) = 2\pi(i - 3/2) + \pi \left(\frac{t - t_i^{(\min)}}{t_i^{(\max)} - t_i^{(\min)}} \right) \quad \text{for } t_i^{(\min)} \leq t < t_i^{(\max)}, \quad (\text{B.7})$$

and $\Phi(t)$ between the central maximum and the right minimum [corresponding to the beginning point of the $(i + 1)$ th global cycle] is given by

$$\Phi(t) = 2\pi(i - 1) + \pi \left(\frac{t - t_i^{(\max)}}{t_{i+1}^{(\min)} - t_i^{(\max)}} \right) \quad \text{for } t_i^{(\max)} \leq t < t_{i+1}^{(\min)}, \quad (\text{B.8})$$

where $t_i^{(\min)}$ is the beginning time of the i th ($i = 1, 2, 3, \dots$) global cycle of $R(t)$ [i.e., the time at which the left minimum of $R(t)$ appears in the i th global cycle], and $t_i^{(\max)}$ is the time at which the maximum of $R(t)$ appears in the i th global cycle. Then, the contributions of the k th microscopic spikes in the i th stripes occurring at the times $t_k^{(s)}$ to $R(t)$ are given by $\cos \Phi_k$, where Φ_k are the global phases at the k th spiking time [i.e., $\Phi_k \equiv \Phi(t_k^{(s)})$]. Microscopic spikes make the most constructive (in-phase) contributions to $R(t)$ when the corresponding global phases Φ_k are $2\pi n$ ($n = 0, 1, 2, \dots$), while they make the most destructive (anti-phase) contribution to $R(t)$ when Φ_k is $2\pi(n - 1/2)$. By averaging the contributions of all microscopic spikes in the i th stripes to $R(t)$, we obtain the pacing degrees P_i of spikes in the i th stripe:

$$P_i = \frac{1}{S_i} \sum_{k=1}^{S_i} \cos \Phi_k \quad (\text{B.9})$$

where S_i is the total number of microscopic spikes in the i th stripe. By averaging M_i of Eq. (B.5) over a sufficiently large number N_s of

stripes, we obtain the statistical–mechanical spiking measure M_s :

$$M_s = \frac{1}{N_s} \sum_{i=1}^{N_s} M_i. \quad (\text{B.10})$$

Here, we follow 3×10^3 global cycles in each realization, and obtain the average occupation degree, the average pacing degree, and the average statistical–mechanical spiking measure via average over 20 realizations.

References

- Achard, S., & Bullmore, E. T. (2007). Efficiency and cost of economical brain functional networks. *PLoS Computational Biology*, 3, e17.
- Bassett, D. S., & Bullmore, E. (2006). Small-world brain networks. *The Neuroscientist*, 12, 512–523.
- Batista, C. A. S., Batista, A. M., de Pontes, J. A. C., Viana, R. L., & Lopes, S. R. (2007). Chaotic phase synchronization in scale-free networks of bursting neuron. *Physical Review E*, 76, 016218.
- Benabid, A. L., Chabardes, S., Mitrofanis, J., & Pollak, P. (2009). Deep brain stimulation of the subthalamic nucleus for the treatment of Parkinson's disease. *The Lancet Neurology*, 8, 67–81.
- Bonifazi, P., Goldin, M., Picardo, M. A., Jorquera, I., Cattani, A., Bianconi, G., et al. (2009). GABAergic hub neurons orchestrate synchrony in developing hippocampal networks. *Science*, 326, 1419–1424.
- Brandes, U. (2001). A faster algorithm for betweenness centrality. *Journal of Mathematical Sociology*, 25, 163–177.
- Brunel, N. (2000). Dynamics of sparsely connected networks of excitatory and inhibitory spiking neurons. *Journal of Computational Neuroscience*, 8, 183–208.
- Brunel, N., & Hakim, V. (1999). Fast global oscillations in networks of integrate-and-fire neurons with low firing rates. *Neural Computation*, 11, 1621–1671.
- Brunel, N., & Hakim, V. (2008). Sparsely synchronized neuronal oscillations. *Chaos*, 18, 015113.
- Brunel, N., & Hansel, D. (2006). How noise affects the synchronization properties of recurrent networks of inhibitory neurons. *Neural Computation*, 18, 1066–1110.
- Brunel, N., & Wang, X.-J. (2003). What determines the frequency of fast network oscillations with irregular neural discharges? I. Synaptic dynamics and excitation–inhibition balance. *Journal of Neurophysiology*, 90, 415–430.
- Buhl, E. H., Tamas, G., & Fisahn, A. (1998). Cholinergic activation and tonic excitation induce persistent gamma oscillations in mouse somatosensory cortex in vitro. *The Journal of Physiology*, 513, 117–126.
- Bullmore, E., & Sporns, O. (2009). Complex brain networks: graph theoretical analysis of structural and functional systems. *Nature Reviews Neuroscience*, 10, 186–198.
- Buzsáki, G. (2006). *Rhythms of the brain*. New York: Oxford University Press.
- Buzsáki, G., Geisler, C., Henze, D. A., & Wang, X.-J. (2004). Interneuron diversity series: circuit complexity and axon wiring economy of cortical interneurons. *Trends in Neurosciences*, 27, 186–193.
- Buzsáki, G., & Wang, X.-J. (2012). Mechanisms of gamma oscillations. *Annual Review of Neuroscience*, 35, 203–225.
- Chklovskii, D. B., Mel, B. W., & Svoboda, K. (2004). Cortical rewiring and information storage. *Nature*, 431, 782–788.
- Connors, B. W., & Gutnick, M. J. (1990). Intrinsic firing patterns of diverse neocortical neurons. *Trends in Neurosciences*, 13, 99–104.
- Csicsvari, J., Hirase, H., Czurko, A., & Buzsáki, G. (1998). Reliability and state-dependence of pyramidal cell–interneuron synapses in the hippocampus: An ensemble approach in the behaving rat. *Neuron*, 21, 179–189.
- Csicsvari, J., Hirase, H., Czurko, A., Mamiya, A., & Buzsáki, G. (1999). Oscillatory coupling of hippocampal pyramidal cells and interneurons in the behaving rat. *The Journal of Neuroscience*, 19, 274–287.
- Fagiolo, G. (2007). Clustering in complex directed networks. *Physical Review E*, 76, 026107.
- Felleman, D. J., & van Essen, D. C. (1991). Distributed hierarchical processing in the primate cerebral cortex. *Cerebral Cortex*, 1, 1–47.
- Fellous, J., & Sejnowski, T. J. (2000). Cholinergic induction of oscillations in the hippocampal slice in the slow (0.5–2 Hz), theta (5–12 Hz) and gamma (35–70 Hz) bands. *Hippocampus*, 10, 187–197.
- Fisahn, A., Pike, F. G., Buhl, E. H., & Paulsen, O. (1998). Cholinergic induction of network oscillations at 40 hz in the hippocampus in vitro. *Nature*, 394, 186–189.
- Freeman, L. C. (1977). A set of measures of centrality based on betweenness. *Sociometry*, 40, 35–41.
- Freeman, L. C. (1978). Centrality in social networks conceptual clarification. *Social Networks*, 1, 215–239.
- Fries, P., Reynolds, J. H., Rorie, A. E., & Desimone, R. (2001). Modulation of oscillatory neuronal synchronization by selective visual attention. *Science*, 291, 1560–1563.
- Geisler, C., Brunel, N., & Wang, X.-J. (2005). Contributions of intrinsic membrane dynamics to fast network oscillations with irregular neuronal discharges. *Journal of Neurophysiology*, 94, 4344–4361.
- Gerhard, F., Pipa, G., Lima, B., Neuenschwander, S., & Gerstner, W. (2011). Extraction of network topology from multi-electrode recordings: Is there a small-world effect? *Frontiers in Computational Neuroscience*, 5, 4.

- Ginzburg, I., & Sompolinsky, H. (1994). Theory of correlations in stochastic neural networks. *Physical Review E*, 50, 3171–3191.
- Golomb, D., & Rinzel, J. (1994). Clustering in globally coupled inhibitory neurons. *Physica D*, 72, 259–282.
- Gulyás, A. I., Hájós, N., & Freund, T. F. (1996). Interneurons containing calretinin are specialized to control other interneurons in the rat hippocampus. *The Journal of Neuroscience*, 16, 3397–3411.
- Gulyás, A. I., Hájós, N., Katona, I., & Freund, T. F. (2003). Interneurons are the local targets of hippocampal inhibitory cells which project to the medial septum. *European Journal of Neuroscience*, 17, 1861–1872.
- Hamani, C., Neimat, J., & Lozano, A. M. (2006). Deep brain stimulation for the treatment of Parkinson's disease. *Journal of Neural Transmission Supplementa*, 70, 393–399.
- Hansel, D., & Mato, G. (2003). Asynchronous states and the emergence of synchrony in large networks of interacting excitatory and inhibitory neurons. *Neural Computation*, 15, 1–56.
- Hansel, D., Mato, G., & Meunier, C. (1994). Synchrony in excitatory neural networks. *Neural Computation*, 7, 307–337.
- Hansel, D., & Sompolinsky, H. (1992). Synchronization and computation in a chaotic neural network. *Physical Review Letters*, 68, 718–721.
- Hilgetag, C. C., Burns, G. A. P. C., O'Neill, M. A., Scannell, J. W., & Young, M. P. (2000). Anatomical connectivity defines the organization of clusters of cortical areas in the macaque monkey and the cat. *Philosophical Transactions of the Royal Society of London B*, 355, 91–110.
- Hodgkin, A. L. (1948). The local electric changes associated with repetitive action in a non-medullated axon. *The Journal of Physiology*, 107, 165–181.
- Ivanchenko, M. V., Osipov, G. V., Shalfeev, V. D., & Kurths, J. (2004). Phase synchronization in ensembles of bursting oscillators. *Physical Review Letters*, 93, 134101.
- Izhikevich, E. M. (2000). Neural excitability, spiking and bursting. *International Journal of Bifurcation and Chaos*, 10, 1171–1266.
- Izhikevich, E. M. (2003). Simple model of spiking neurons. *IEEE Transactions on Neural Networks*, 14, 1569–1572.
- Izhikevich, E. M. (2004). Which model to use for cortical spiking neurons? *IEEE Transactions on Neural Networks*, 15, 1063–1070.
- Izhikevich, E. M. (2007). *Dynamical systems in neuroscience*. Cambridge: MIT Press.
- Izhikevich, E. M. (2010). Hybrid spiking models. *Philosophical Transactions of the Royal Society A*, 368, 5061–5070.
- Jinno, S., Klausberger, T., Marton, L. F., Dalezios, Y., Roberts, J. D. B., Fuentealba, P., et al. (2007). Neuronal diversity in GABAergic long-range projections from the hippocampus. *The Journal of Neuroscience*, 27, 8790–8804.
- Kaiser, M., & Hilgetag, C. C. (2006). Nonoptimal component placement, but short processing paths, due to long-distance projections in neural systems. *PLoS Computational Biology*, 2, e95.
- Kim, S.-Y., & Lim, W. (2013). Sparsely-synchronized brain rhythm in a small-world neural network. *Journal of the Korean Physical Society*, 63, 104–113.
- Kim, S.-Y., & Lim, W. (2014). Realistic thermodynamic and statistical-mechanical measures for neural synchronization. *Journal of Neuroscience Methods*, 226, 161–170.
- Kim, S.-Y., & Lim, W. (2015a). Fast sparsely synchronized brain rhythms in a scale-free neural network. *Physical Review E*, 92, 022717.
- Kim, S.-Y., & Lim, W. (2015b). Effect of small-world connectivity on fast sparsely synchronized cortical rhythms. *Physica A*, 421, 109–123.
- Kwon, O., & Moon, H. T. (2002). Coherence resonance in small-world networks of excitable cells. *Physics Letters A*, 298, 319–324.
- Lago-Fernández, L. F., Huerta, R., Corbacho, F., & Sigüenza, J. A. (2000). Fast response and temporal coherent oscillations in small-world networks. *Physical Review Letters*, 84, 2758–2761.
- Larimer, P., & Strowbridge, B. W. (2008). Nonrandom local circuits in the dentate gyrus. *The Journal of Neuroscience*, 28, 12212–12223.
- Lim, W., & Kim, S.-Y. (2011). Statistical-mechanical measure of stochastic spiking coherence in a population of inhibitory subthreshold neuron. *Journal of Computational Neuroscience*, 31, 667–677.
- Lizier, J. T., Pritam, S., & Prokopenko, M. (2011). Information dynamics in small-world Boolean networks. *Artificial Life*, 17, 293–314.
- Logothetis, N. K., Pauls, J., Augath, M. A., Trinath, T., & Oeltermann, A. (2001). Neurophysiological investigation of the basis of the fMRI signal. *Nature*, 412, 150–157.
- Longtin, A. (1995). Synchronization of the stochastic Fitzhugh-Nagumo equations to periodic forcing. *Nuovo Cimento D*, 17, 835–846.
- Longtin, A. (2000). Stochastic aspects of neural phase locking to periodic signals. In S. Kim, K. J. Lee, & W. Sung (Eds.), *Stochastic dynamics and pattern formation in biological and complex systems* (pp. 219–239). New York: AIP.
- Mathewson, K. E., Prudhomme, C., Fabiani, M., Beck, D. M., Lleras, A., & Gratton, G. (2012). Making waves in the stream of consciousness: Entraining oscillations in EEG alpha and fluctuations in visual awareness with rhythmic visual stimulation. *Journal of Cognitive Neuroscience*, 24, 2321–2333.
- Melzer, S., Michael, M., Caputi, A., Eliava, M., Fuchs, E. C., Whittington, M. A., et al. (2012). Long-range-projecting gabaergic neurons modulate inhibition in hippocampus and entorhinal cortex. *Science*, 23, 1506–1510.
- Milton, J., & Jung, P. (Eds.) (2003). *Epilepsy as a dynamic disease*. Berlin: Springer-Verlag.
- Newman, M. E. J. (2001). Scientific collaboration networks. II. Shortest paths, weighted networks, and centrality. *Physical Review E*, 64, 016132.
- Nishikawa, T., Motter, A. E., Lai, Y.-C., & Hoppensteadt, F. C. (2003). Heterogeneity in oscillator networks: are smaller worlds easier to synchronize? *Physical Review Letters*, 91, 014101.
- Ozer, M., Perc, M., & Uzuntarla, M. (2009). Stochastic resonance on Newman-Watts networks of Hodgkin-Huxley neurons with local periodic driving. *Physics Letters A*, 373, 964–968.
- Riecke, H., Roxin, A., Madrugá, S., & Solla, S. (2007). Multiple attractors, long chaotic transients, and failure in small-world networks of excitable neurons. *Chaos*, 17, 026110.
- Rosenblum, M. G., & Pikovsky, A. S. (2004a). Controlling synchronization in an ensemble of globally coupled oscillators. *Physical Review Letters*, 92, 114102.
- Rosenblum, M. G., & Pikovsky, A. S. (2004b). Delayed feedback control of collective synchrony: An approach to suppression of pathological brain rhythms. *Physical Review E*, 70, 041904.
- Roxin, A., Riecke, H., & Solla, S. A. (2004). Self-sustained activity in a small-world network of excitable neurons. *Physical Review Letters*, 92, 198101.
- San Miguel, M., & Toral, R. (2000). Stochastic effects in physical systems. In J. Martínez, R. Tiemann, & E. Tirapegui (Eds.), *Instabilities and nonequilibrium structures VI* (pp. 35–130). Dordrecht: Kluwer Academic Publisher.
- Scannell, J. W., Burns, G. A. P. C., Hilgetag, C. C., O'Neill, M. A., & Young, M. P. (1999). The connective organization of the cortico-thalamic system of the cat. *Cerebral Cortex*, 9, 277–299.
- Shanahan, M. (2008). Dynamical complexity in small-world networks of spiking neurons. *Physical Review E*, 78, 041924.
- Shi, L., Niu, X., & Wan, H. (2015). Effect of the small-world structure on encoding performance in the primary visual cortex: an electrophysiological and modeling analysis. *Journal of Comparative Physiology A*, 201, 471–483.
- Shimazaki, H., & Shinomoto, S. (2010). Kernel bandwidth optimization in spike rate estimation. *Journal of Computational Neuroscience*, 29, 171–182.
- Sik, A., Ylinen, A., Penntonen, M., & Buzsáki, G. (1994). Inhibitory CA1-CA3-hilar region feedback in the hippocampus. *Science*, 265, 1722–1724.
- Song, S., Sjöström, P. J., Reigl, M., Nelson, S., & Chklovskii, D. B. (2005). Highly nonrandom features of synaptic connectivity in local cortical circuits. *PLoS Biology*, 3, e68.
- Sporns, O. (2011). *Networks of the brain*. Cambridge: MIT Press.
- Sporns, O., & Honey, C. J. (2006). Small worlds inside big brains. *Proceedings of the National Academy of Sciences of the United States of America*, 103, 19219–19220.
- Sporns, O., Tononi, G., & Edelman, G. M. (2000). Theoretical neuroanatomy: relating anatomical and functional connectivity in graphs and cortical connection matrices. *Cerebral Cortex*, 10, 127–141.
- Strogatz, S. H. (2001). Exploring complex networks. *Nature*, 410, 268–276.
- Tateno, T., Harsch, A., & Robinson, H. P. C. (2004). Threshold firing frequency-current relationships of neurons in rat somatosensory cortex: type 1 and type 2 dynamics. *Journal of Neurophysiology*, 92, 2283–2294.
- Tiesinga, P. H. E., Fellous, J.-M., Jose, J. V., & Sejnowski, T. J. (2001). Computational model of carbachol-induced delta, theta, and gamma oscillations in the hippocampus. *Hippocampus*, 11, 251–274.
- van Vreeuwijk, C., Abbott, L. F., & Ermentrout, G. B. (1994). When inhibition not excitation synchronizes neural firing. *Journal of Computational Neuroscience*, 1, 313–321.
- Viana, R. L., Batista, A. M., Batista, C. A. S., de Pontes, J. C. A., Silva, F. A. Dos S., & Lopes, S. R. (2012). Bursting synchronization in networks with long-range coupling mediated by a diffusing chemical substance. *Communications in Nonlinear Science and Numerical Simulation*, 17, 2924–2942.
- Wang, X.-J. (2003). Neural oscillations. In L. Nadel (Ed.), *Encyclopedia of cognitive science* (pp. 272–280). London: MacMillan.
- Wang, X.-J. (2010). Neurophysiological and computational principles of cortical rhythms in cognition. *Physiological Reviews*, 90, 1195–1268.
- Wang, X.-J., & Buzsáki, G. (1996). Gamma oscillations by synaptic inhibition in a hippocampal interneuronal network. *The Journal of Neuroscience*, 16, 6402–6413.
- Wang, Q., Duan, Z., Perc, M., & Chen, G. (2008). Synchronization transitions on small-world neuronal networks: Effects of information transmission delay and rewiring probability. *Europhysics Letters*, 83, 50008.
- Wang, Q., Perc, M., Duan, Z., & Chen, G. (2010). Impact of delays and rewiring on the dynamics of small-world neuronal networks with two types of coupling. *Physica A*, 389, 3299–3306.
- Wang, X.-J., & Rinzel, J. (1992). Alternating and synchronous rhythms in reciprocally inhibitory model neurons. *Neural Computation*, 4, 84–97.
- Watts, D. J. (2003). *Small worlds: the dynamics of networks between order and randomness*. Princeton University Press.
- Watts, D. J., & Strogatz, S. H. (1998). Collective dynamics of 'small-world' networks. *Nature*, 393, 440–442.
- White, J., Chow, C. C., Ritt, J., Soto-Trevino, C., & Kopell, N. (1998). Synchronization and oscillatory dynamics in heterogeneous, mutually inhibited neurons. *Journal of Computational Neuroscience*, 5, 5–16.
- Whittington, M. A., Traub, R. D., Kopell, N., Ermentrout, B., & Buhl, E. H. (2000). Inhibition-based rhythms: Experimental and mathematical observation on network dynamics. *International Journal of Psychophysiology*, 38, 315–336.
- Will, U., & Berg, E. (2007). Brain wave synchronization and entrainment to periodic acoustic stimuli. *Neuroscience Letters*, 424, 55–60.
- Young, M. P. (1993). The organization of neural systems in the primate cerebral cortex. *Proceedings of Royal Society London B*, 252, 13–18.
- Yu, S., Huang, D., Singer, W., & Nikolic, D. (2008). A small world of neuronal synchrony. *Cerebral Cortex*, 18, 2891–2901.